UNIVERSITY OF CAPE TOWN

Division of Biomedical Engineering

Department of Human Biology

University of Cape Town

Experimental and Computational Study of the Mechanics of Chikungunya

By

Thabang Ofentse Matseke

MTSTHA077

Dissertation

submitted to

THE UNIVERSITY OF CAPE TOWN

In fulfilment of the requirements for the degree:

MSc in Biomedical Engineering

Supervisor: Prof. Thomas Franz

Date: 15 April 2021

Declaration

I, Thabang Ofentse Matseke, hereby declare that the work on which this dissertation/thesis is based is my original work (except where acknowledgements indicate otherwise) and that neither the whole work nor any part of it has been, is being, or is to be submitted for another degree in this or any other university.

I empower the university to reproduce for the purpose of research either the whole or any portion of the contents in any manner whatsoever.

Signature: 

Date: 15 April 2021

Abstract

Diseases outbreaks caused by infections from microorganisms like human immunodeficiency virus (HIV), influenza virus, Ebola virus, Zika virus, dengue virus, and malaria have infected millions of people in Africa. In Africa, viruses with a viral envelope, i.e. enveloped viruses, like HIV and influenza, cause thousands of deaths each year yet no cure exists. It has been proposed that the mechanical properties of enveloped viruses may play a role in viral entry into host cells. This dissertation aimed to study experimentally and computationally the mechanical properties of chikungunya virus to enable mechanobiological investigations of interactions between the chikungunya virus, and other enveloped viruses, and host cells involved in the infection process.

The chikungunya virus strain used was the S27-African prototype and the virions underwent nanoindentation using atomic force microscopy (AFM). Tests were conducted in pH = 7.4 and 6.0 representing neutral extracellular and acidic endosomal environments, respectively, the latter promoting viral fusion. The height of the virion was recorded using AFM tapping mode before and after the indentation. The indentation tests were performed using AFM force spectroscopy mode. The spring constant of the virus was determined from the force-displacement data for an indentation force between 0.1 and 0.4 nN. The height and spring constant of the virions were considerably larger in the neutral extracellular environment (h_v = 57.8 ± 0.6 nm; k_v = 0.035 ± 0.003 N/m) than in the acidic endosomal environment (h_v = 46.0 ± 0.8 nm; k_v = 0.047 ± 0.003 N/m). It is proposed that the acidification of the environment caused partial or full dissociation of the glycoproteins from the membrane. Due to the hydrophobicity of the membrane and the way the glycoproteins are embedded, the membrane may also have dissociated from the capsid.

A computational three-dimensional geometry of a chikungunya virus-like particle (VLP) was generated from cryogenic electron microscope (cryo-EM) images and developed into a finite element (FE) model to simulate nanoindentation tests. The VLP was represented as linear-elastic material. The calibration of the model using data from the indentation experiments in neutral extracellular environment predicted an elastic modulus of the chikungunya VLP of E = 2.9, 3.5 and 4.0 MPa for a Poisson's ratio of ν = 0.4, 0.35 and 0.3, respectively.

The experimental part of this dissertation provides new information on the mechanical properties of chikungunya virus and on possible mechanical and conformational changes of the virus during the infection process. The microstructural FE model, combined with the experimental data, can facilitate future studies into the mechanics and mechanobiology of virion-host cell interactions during infection.

Acknowledgements

This research was financially supported by the National Research Foundation (NRF) of South Africa and the South African Medical Research Council (SAMRC). All findings, views, conclusions, and recommendations expressed in the dissertation are those of the author and do not represent the views, opinions, or conclusions of the NRF and SAMRC. Funding for an international visit was provided by the Max & Lillie Sonnenberg Scholarship. Thank you to the Nsthole Foundation and Boikgantsho Consulting and Events (BCE) for the funding received to undertake this project. Without your support, my dream of an MSc would not have been realised.

From the Molecular Biophysics Group at the Zernike Institute for Advanced Materials at the University of Groningen, I would like to thank: Prof. Wouter Roos for providing me the opportunity for the research visit and the use of the AFM facilities, and advising me on AFM and virus mechanics; Dr. Ignacio López de Blas for teaching me how to perform experiments using AFM and the insightful lessons on life, art and music; Mr Guus van der Borg for advising me on virus preparation and donating chikungunya virus samples for the AFM experiments.

From the Mechanobiology lab at the University of Cape Town, thank you to; Dr. Tamer Abdalrahman and Dr. Kevin Sack for assisting me with the development of the geometric reconstruction and computational modelling; Mr. Chimwemwe Msosa, Mr. Dodzi Motchon, Mr. John Nchejane and Ms. Juliet Nagawa for helping me with Abaqus/CAE and Simpleware ScanIP; and Ms Ghodeejah Higgins for teaching me about statistics.

Thank you to my supervisor, Prof. Thomas Franz, from the Mechanobiology lab at the University of Cape Town, for your patience, guidance, encouragement, and advice throughout the project. Your support over the years has been invaluable; without this, this MSc would not have been achievable.

To Ms Elizabeth Kruse from the Mechanobiology lab at the University of Cape Town, thank you for being an amazing friend and mentor. Your support throughout my project, academically and personally, is immeasurable. It has been such a pleasure to know and learn from you.

Thank you to my family: my mother, Keabetswe Matseke, and my sister, Motlalekgomo Matseke, for being my grounding force and sounding board; and the rest of my family, the Matsekes and the Mores, for their constant love and support.

Table of Contents

1. Introduction and Problem Identification 1
   1.1. Chikungunya Virus Prevalence, Transmission and Pathogenesis 1
   1.2. Morphology of Chikungunya Virus 3
   1.3. Chikungunya Virus Lifecycle 4
   1.4. Chikungunya Virus-Like Particles 7
   1.5. Morphology of the Human Cell Membrane 7
   1.6. Mechanical Virology 8
      1.6.1. Mechanical Assessment of Virions using Atomic Force Microscopy 11
   1.7. Image-based 3D Modelling of Viruses 14
   1.8. Finite Element Modelling of Viruses 17
   1.9. Problem Identification and Limitations of Past Research 19
   1.10. Aim and Objectives 19
2. Mechanical Assessment of Chikungunya Virus-Like Particles in different Endosomal Environments 21
   2.1. Introduction 21
   2.2. Materials and Methods 21
      2.2.1. Virus Material and Preparation 21
      2.2.2. Hydrophobic Glass Coverslip and Sample Preparations 23
      2.2.3. pH Adjustment 25
      2.2.4. AFM Indentation Tests 26
      2.2.5. Data Analysis 28
      2.2.6. Statistical Analysis 30
   2.3. Results 30
      2.3.1. Height 31
      2.3.2. Spring Constant 33
      2.3.3. Correlation between Height and Spring Constant 34
   2.4. Discussion 35
      2.4.1. Height 36
      2.4.2. Spring Constant 37
      2.4.3. Correlation between Height and Spring Constant 38
3. Development of 3D Geometric Model and Computational Simulations of Chikungunya Virions 39
   3.1. Introduction 39
   3.2. Materials and Methods 39
      3.2.1. Geometric Modelling 39

3.2.2. Finite Element Modelling 41
3.3. Results 47
3.3.1. Development of 3D Geometric Models 47
3.3.2. Finite Element Modelling 49
3.4. Discussion 51
3.4.1. Development of 3D Geometric Models 51
3.4.2. Finite Element Modelling 51
4. Conclusions and Recommendations 53
4.1. Conclusions 53
4.1.1. Mechanical Assessment of Chikungunya Virions 53
4.1.2. Development of 3D Geometric Model and Computational Simulations of Chikungunya Virions 54
4.2. Recommendations 54
4.2.1. Imaging of Chikungunya Virions 54
4.2.2. Investigation of Virion Cross-Section 55
4.2.3. Expand Experimental Sample Size 55
4.2.4. Standardisation of Testing Environment 55
4.2.5. Variation of Constitutive Law 55
4.2.6. Variation of Material Properties 56
4.2.7. Refinement of the Internal Virion Geometry 56
5. References 57

List of Abbreviations

2D	Two-dimensional
3D	Three-dimensional
AFM	Atomic force microscopy
ANOVA	Analysis of variance
CCMV	Cowpea chlorotic mottle virus
CHIKV	Chikungunya
Cryo-EM	Cryogenic electron microscopy
CT	Cytoplasmic tail
DEET	N, N-diethyl-3-methylbenzamide
DNA	Deoxyribonucleic acid
DRC	Democratic Republic of Congo
ECSA	East-Central South Africa
EDTA	Ethylenediaminetetraacetic acid
EE	Early endosomal
EI	Expansion intermediate
EM	Electron microscopy
ER	Endoplasmic reticulum
FE	Finite element
FD	Force-displacement
GFP	Green fluorescent protein
H-II	Head II
HA	Hemagglutinin
HBV	Hepatitis B virus
HDMS	Hexamethyldisilazane
HIV	Human immunodeficiency virus
Hoc	Highly immunogenic outer capsid protein
icaridin	1-piperidinecarboxylic acid, 2-(2-hydroxyethyl)-1-methylpropylester
IR3535	3-[N-acetyl-N-butyl]-aminopropionic acid ethyl ester
KCl	Potassium chloride
KH_2PO_4	Potassium dihydrogenphosphate
KOH	Potassium hydroxide
LE	Late endosomal
M1	Matrix protein
MES	2-(N-Morpholino)ethanesulfonic acid
MVM	Parvovirus minute virus of mice
NA	Neuraminidase
NaCl	Sodium chloride
Na_2HPO_4	Sodium hydrogen phosphate
NaOH	Sodium hydroxide
NV	Norwalk virus
P-I	Prohead I
P-II	Prohead II
PBS	Phosphate-buffered saline
pH	Potential of hydrogen
RNA	Ribonucleic acid
RNP	Ribonucleoprotein
SD	Standard deviation
SEM	Standard error of the mean
Soc	Small outer capsid protein

T number	Triangulation number
TM	Transmembrane
WT	Wild-type
VLP	Virus-like particle
vs	Versus

Symbols

α	Proportionality factor
Å	Angstrom
E_i	Elastic modulus of the indenter
E_s	Elastic modulus of the substrate
E_t	Elastic modulus of virion calculated using the thin shell model
E_v	Elastic modulus of virion
F_i	Force applied on virion during imaging
h_v	Actual cross-sectional height of virion
h_{xs}	Cross-sectional height of virion from imaging
k_c	Spring constant of the cantilever
k_t	Spring constant of total system
k_v	Spring constant of virus
R	Radius of the virus
ν_i	Poisson's ratio of the indenter
ν_s	Poisson's ratio of substrate
ν_v	Poisson's ratio of virion

List of Tables

Table 2-1: Spring constant of chikungunya virus compared to other viruses. 37
Table 3-1: Types and number of elements for the components in the model. 42
Table 3-2: Material properties of the components in the model. 43
Table 3-3: Elastic modulus of chikungunya virus compared to other viruses. 52

List of Figures

Figure 1-1: Countries/territories with reported chikungunya virus cases as of 2019. The map shows the countries/territories where chikungunya virus cases have been reported as of 17 September 2019. The map does not include countries/territories where only imported cases have been documented. Reproduced from Centers for Disease Control and Prevention (2019b).....2

Figure 1-2: Simple enveloped virion structure. A simple virion structure consists of the enveloped glycoproteins embedded along the surface of the membrane. The matrix protein is found on the inside the membrane which surrounds the nucleocapsid shell. The nucleocapsid protects the viral genome, which is comprised of an RNA or DNA strand(s).....3

Figure 1-3: Morphology of chikungunya virus. The (a) external and (b) internal morphology of chikungunya virus. The black triangle in (a) highlights one icosahedral unit. The structural layers are illustrated according to the colour scale in (c). Scale: 1 Angstrom (Å) = 0.1 nm. With permission from Yap et al. (2017). 4

Figure 1-4: A schematic of fusogenic viral entry. (a) A non-specific enveloped virion adheres to the cell membrane and initiating an interaction between the viral glycoproteins and host cell receptors. Fusion of the membranes can either be (b) initiated immediately after contact between the viral glycoproteins and host cell receptors or (c & d) the host cell membrane will partially wrap the virion, and then fusion will occur. Adapted with permission from Chou (2007).....5

Figure 1-5: A schematic of endocytotic viral entry. (a) A non-specific enveloped virion adhering to the cell membrane and (b) an interaction between the viral glycoproteins and host cell receptors is formed. (c) The host cell membrane then wraps and (d) internalizes the virion. Adapted with permission from Chou (2007). 5

Figure 1-6: Lifecycle of a chikungunya virion. The virion lifecycle involves docking with the host receptor protein, then wrapping of the virion to form the endosome. Lowering of pH of endosomal environment induces viral genome release. This is followed by synthesis of viral components which will then be assembled into complete viral units and bud from the host cell. 6

Figure 1-7: Morphology of a chikungunya virion vs. a chikungunya VLP. An illustration of the general structure of a) a chikungunya virion and b) a chikungunya VLP. VLPs do not contain the viral genome. 7

Figure 1-8: Fluid mosaic model of the cell membrane. The fluid mosaic model includes a phospholipid bilayer, carbohydrates, cholesterols and various other membrane proteins. With permission from Pietzsch (2004).....8

Figure 1-9: The expansion of the Bacteriophage HK97 virion during maturation. The Δ-domain, which is responsible for capsid assembly, is cleaved from the Prohead I form to transition into the Prohead

II form. The capsid undergoes further expansion to reach the mechanically stable Head II form. Adapted with permission from Roos et al. (2012). 9
Figure 1-10: Two-step uncoating of the influenza virus. In the early endosomal (EE) environment, the envelope glycoproteins are softened. This was followed by the late endosomal (LE) environment, which was indicated by disassembly of the M1 layer its disassociation from the lipid layer in order to release the viral genome. With permission from Li et al. (2014). 10
Figure 1-11: Simple AFM setup. The red line indicates the path travelled by the cantilever, and the arrow indicates the direction. As the cantilever deflects in the z-axis, it moves along the topography of the sample, and these changes are recorded on the photodiode. 11
Figure 1-12: Topography map of an enveloped virion. The virion imaged is spherically shaped. The units for all axes are nm. 11
Figure 1-13: Imaging using jumping/pulsed mode. The arrow indicates the direction the cantilever scans the sample. The inset is the force vs extension curve measured at every pixel. Point 1 is the maximum height of the cantilever before approaching the sample. Point 2 is the maximum deflection point of the cantilever. Point 3 is the maximum distance between the sample and the tip. Point 4 is the point of contact between the tip and sample. 12
Figure 1-14: Imaging using dynamic mode. The cantilever scans over the sample in the direction shown by the arrow and oscillates at a user-specified fixed amplitude. 13
Figure 1-15: Cantilever artefacts. The image is taken of a chikungunya virus sample. The particles enclosed in red circles all have a similar, irregular shape which may be an indicator of impurities attached to the tip. 14
Figure 1-16: Reconstruction of a typical influenza type B virion. A typical type B virion has a diameter of 130 nm. The RNP (red) is surrounded by the M1 layer (purple). The envelope glycoproteins (HA and NA), indicated in pink, are arranged on the surface of the M1 layer. With permission from Katz et al. (2014). 14
Figure 1-17: Reconstruction of mutant bacteriophage T4 capsids. Mutant bacteriophage T4 wild-type (WT) a) prolate capsid and b) isometric capsid geometries a presented at 3.3 Å resolution. The prolate capsid is characterised by T_{ends} = 13 for the icosahedral ends and T_{mid} = 20 for the elongated section. The icosahedral capsid is characterised by T = 13 and has a diameter of 86 nm. The different colours represent the proteins on the outer surface of the capsids. Gp23*, gp24*, Hoc, and Soc are coloured blue, magenta, yellow, and white, respectively. With permission from Chen et al. (2017). 15
Figure 1-18: A reconstructed model of an HIV virion. a) The capsid is illustrated in red and the virion shell in blue. The image was reconstructed using UCSF Chimera. b) The reconstructed continuous 3D geometric model was created using Simpleware ScanIP. With permission from Kruse (2017). 16

Figure 1-19: Reconstruction of chikungunya VLP. The image illustrates the reconstructed a) VLP and b) nucleocapsid and c) cross-section of the VLP. The envelope glycoproteins are visible on the surface of the VLP. The black triangle in (a) highlights one icosahedral unit. The structural layers are illustrated according to the colour scale in (c). Scale: 1 Angstrom (Å) = 0.1 nm. With permission from Yap et al. (2017). 16

Figure 1-20: Finite element simulation for indentation of immature and mature virions. Finite element simulation for indentation of (a) immature and (b) mature virions, both with an outside diameter of 50 nm. The immature virions have a shell thickness of 20 nm while the mature virions have a shell thickness of 4 nm. With permission from Kol et al. (2006). 17

Figure 1-21: Indentation of spherical and icosahedral shaped Bacteriophage λ capsid shells using finite element simulation. The finite element models setup of a) a spherical shaped Bacteriophage λ capsid and b) icosahedral shaped Bacteriophage λ capsid. The image includes the comparison of the force-indentation curves of the experimental data and finite element simulation results with various Young's moduli for the c) spherical shaped and d) icosahedral shaped capsid. With permission from Ahadi et al. (2009). 18

Figure 1-22: Comparison of force-indentation curves of Hepatitis B. The graph represents indentation curves from experimental data (thin lines), the average of these curves (thick green line) with error bars (SEM). The graph also represents the indentation behaviour of 3D topographically detailed models (thick blue line) and thin shell models with FvK 330 (thick red line). The capsids are indented along the T = 4 symmetry axis. With permission from Roos et al. (2010). 19

Figure 2-1: The structural breakdown of chikungunya virus. An estimate of the structure of the virion was determined by measuring EM data of chikungunya virions. The image indicates the diameter of the RNA, capsid, membrane and whole virion (E1/E2 protein). Adapted with permission from Yap et al. (2017). 22

Figure 2-2: Illustration of the elution process followed to remove sucrose and calcium from the sample. In a) the PD MiniTrap G-25 column was prepared by removing the top and bottom cap. This was followed by b) column equilibration where +/-8 ml of PBS was allowed to flow through. In c) sample application, the sample (shown in orange) was added the column followed by the 475 µl of PBS. In d) the eluate (shown in beige) was collected and used for testing. 23

Figure 2-3: AFM sample holder with the sample. The AFM sample holder secures the substrate, ensuring there was no movement during the nanoindentation experiments. 24

Figure 2-4: JPK Nanowizard 3 Ultra Speed in the acoustic hood. The acoustic hood was the housing unit and responsible for temperature control throughout the experiments. 26

Figure 2-5: Isolated chikungunya virion on a glass coverslip. The picture represents Test 17 of the virion a) before and b) after the nanoindentation experiment in PBS with with graphs representing the respective cross-sectional height. The black horizontal line on the image indicates where the cross-section was obtained. A nanoindentation test was first performed on the glass coverslip (dark) then the centre of the virion (bright). The scale bar is indicated on the right of the picture. 27
Figure 2-6: Force-displacement curve for a) the glass coverslip and b) the virion. The graphs represent Test 1 of the virions tested in MES. 28
Figure 2-7: Force-displacement curve with a linear fit for Test 21 of the virions tested in PBS. The linear fit of the graph was between 0.1 and 0.4 nN. The spring constant of the total system, determined by the slope of the linear fit, was $kt = 0.01896$ N/m. 28
Figure 2-8: Force-displacement curve with two linear fit lines. The graph represents Test 18 of the nanoindentation experiments of the virions in PBS. The first linear fit (red) of the graph was between 0.1 and 0.4 nN. The second linear fit (green) was between 0.4 nN and the breaking point. The virion spring constant of Test 18 using the first linear fit (red) was kv= 0.035 N/m while the spring constant of the virion using the second linear fit (green) was kv= 0.077 N/m. 29
Figure 2-9: Histogram and Gaussian's curve of the height of the virions tested in PBS and MES. The histogram represents the actual heights of the virions tested in PBS and MES. The actual height of the virions in PBS was 57.8 ± 3.0 nm and in MES was 46.0 ± 5.1 nm. 31
Figure 2-10: A bar graph of the actual height of the virions tested in PBS and MES before and after the nanoindentation experiments. The actual height of the virions in PBS was 48.7 ± 10.3 nm and in MES was 41.6 ± 4.0 nm. The error bars indicate SEM. *p = < .05, **p = < .005, ***p = < .0005. 31
Figure 2-11: A bar graph representing the actual height of virions tested in PBS and MES for experiment 1 and 2. The virions were tested in PBS, the buffer was then removed, and MES was added for further testing. The height of the virions in PBS was 55.8 ± 3.7 nm and in MES was 47.2 ± 4.3 nm. The error bars indicate SEM. *p = < .05, **p = < .005, ***p = < .0005. 32
Figure 2-12: Histogram and Gaussian's curve representing the spring constant of the virions tested in PBS and MES. The histogram represents the spring constant of the virions tested in PBS and MES. The spring constant of the virions in PBS 0.035 ± 0.012 N/m and MES was 0.047 ± 0.017 N/m. 33
Figure 2-13: A bar graph representing spring constant of the virions tested in PBS (slope 1 and 2) and MES. For experiment 1, the spring constant of the virions in PBS slope 1 was 0.035 ± 0.012 N/m, PBS slope 2 was 0.061 ± 0.021 N/m and in MES was 0.047 ± 0.017 N/m. For experiment 2, the spring constant for PBS slope1 was 0.033 ± 0.010 N/m, PBS slope 2 was 0.066 ± 0.015 N/m and in MES was 0.045 ± 0.015 N/m. The error bars indicate SEM. *p = < .05, **p = < .005, ***p = < .0005. 34

Figure 2-14: Correlation of height and spring constant (slope 1) for the virions tested in PBS. The Pearson Correlation test indicated there was no correlation between the heights and spring constant of the virions tested in PBS. The p-value was .46, and R^2 was .026.....35
Figure 2-15: Correlation of height and spring constant (slope 1) for the virions tested in MES. The Pearson Correlation test indicated there was no correlation between the heights and spring constant of the virions tested in MES. The p-value was .13, and R^2 was .063. 35
Figure 2-16: Response of envelope glycoproteins due to an external force. a) The indenter makes contact with the virion. b) The indenter pushes/squashes the envelope proteins. With permission from Schaap et al. (2012).....36
Figure 3-1: Cryo-EM image slice of chikungunya VLP. The EM data, generated by Jin et al. (2015), was found in Protein Data Bank Japan (EMDB-6466). From Protein Data Bank Japan (2015).....39
Figure 3-2: Cross-section view of the geometric model. The image displays the model a) before and b) after the "fill" function was applied.....40
Figure 3-3: Cross-section of the filled model with discontinuities. The red circles indicate discontinuities found in the model after the "fill" function was performed.....40
Figure 3-4: FE model for simulation of nanoindentation experiment comprising reconstructed VLP (green), indenter sphere and rectangular substrate (both blue). 41
Figure 3-5: The computational model, including mesh. The spherical indenter has 139 elements, and the rectangular substrate has 9 elements. The reconstructed VLP had a diameter of 63 nm. The substrate was a 100 nm × 100 nm × 20 nm rectangular body. The indenter was a sphere with a diameter of 10 nm. 42
Figure 3-5: The coordinate system of the model. The model employs the cylindrical coordinate system represented by the T_C-, Z_C- and R_C-axis which corresponds with the X-, Y-, and Z-axis from the default rectangular coordinate system. 43
Figure 3-6: Illustration of boundary conditions. a) Cross-sectional view of the indenter, VLP and substrate, showing the boundary conditions applied to the reference point of indenter and substrate, respectively, indicated by the red arrows, and to internal nodes in the cross-sectional surface of the VLP. b) Boundary conditions on surface nodes of VLP. 45
Figure 3-7: Force-displacement curve for the first VLP tested in PBS. Displayed were the data points used to interpolate the displacements at an indentation force of 0.1 nN and 0.4 nN. The coordinates are shown as (X; Y).....46
Figure 3-8: Force-displacement curve with a straight-line fit. The curve is indicated by the dotted blue line, and the straight-line fit is indicated by the orange line. The straight line is fit between 0.1 and 0.4 nN.....47

Figure 3-9: The 3D geometric model of a chikungunya VLP reconstructed using UCSF Chimera from cryo-EM data generated by Jin et al. (2015). 48
Figure 3-10: Meshed 3D geometric model of chikungunya VLP. The model has 63,439 four-node tetrahedral shaped elements 48
Figure 3-12: Cross-sectional view of the computational simulation from the start of the simulation to the maximum indentation of the VLP illustrating the deformation and associated colour-coded stress distribution in the VLP. The model was calibrated for a Poisson's ratio of ν_v = 0.3, 0.35 and 0.4. The indenter is positioned 1.265 nm above the VLP, and the maximum indenter load was 22 nm. The VLP (blue) is indented by the indenter (grey). The colour-coded mechanical stress scale (MPa) is indicated on the right. 49
Figure 3-13: Force-displacement curves for the predicted elastic moduli. The FD curves for a) Ev = 4 MPa, b) Ev = 3.5 MPa and c) Ev = 2.9 MPa for νv = 0.3, 0.35 and 0.4. The curves for νv = 0.3, 0.35 and 0.4 are indicated with blue squares, oranges circles and grey triangles, respectively. 50
Figure 3-14: Force-displacement curves for the nanoindentation experiments and computational simulations. The FD curves representing the experimental results for the VLPs tested in PBS are indicated by the thin lines. The FD curves from the computational simulations are indicated by the thick lines. The curves from the computational simulations represented for Ev = 2.9 MPa and νv = 0.4 (yellow stars), Ev = 3.5 MPa and νv = 0.35 (purple circles), and Ev = 4 MPa and νv = 0.3 (green squares). 50

1. Introduction and Problem Identification

The chikungunya virus (CHIKV) is an alphavirus and exhibits similar clinical signs as the disease caused by dengue and Zika virus. Infection with the chikungunya virus causes fever, muscle pain, headache, rash, nausea and fatigue. It can also cause severe joint pain (World Health Organization 2017).

Chikungunya virus is transmitted by infected yellow fever mosquitos (Aedes aegypti) or Asian tiger mosquitos (Aedes albopictus), which are also responsible for transmitting the dengue and Zika virus (Centers for Disease Control and Prevention 2019a, Schwartz and Albert 2010, World Health Organization 2019b). The chikungunya virus can also be transmitted from an infected mother to the foetus during pregnancy (Schwartz and Albert 2010).

1.1. Chikungunya Virus Prevalence, Transmission and Pathogenesis

Before the 2000s, human infections with the chikungunya virus occurred at relatively low levels and mainly in Africa. However, there was a large outbreak in Kenya in 2004 (Bordi *et al.* 2015, World Health Organization 2017). During 2005/2006, the outbreak in Africa led to an outbreak on an island in the Indian Ocean that affected nearly 40% of the population and outbreaks in India, Indonesia, Maldives, Myanmar and Thailand where over 1.9 million cases have been reported (Wikan *et al.* 2012, World Health Organization 2017). The outbreaks in Africa and Asia were followed by the first transmission in Europe in 2007 (World Health Organization 2017).

Four main lineages have been reported for the chikungunya virus: West Africa lineage, Asian lineage, East-Central South Africa (ECSA) lineage, and Indian Ocean lineage (Bordi *et al.* 2015). The ECSA lineage is responsible for the outbreak in Kenya, India and Southeast Asia in 2004-2006 (Wikan *et al.* 2012). The Indian Ocean lineage emerged in India and the Indian Ocean islands between 2005 and 2008 and descends from the ECSA lineage.

Before 2004, yellow fever mosquitos mainly transmitted the chikungunya virus; however, during the 2004-2006 outbreak, the virus adapted to transmission by Asian tiger mosquitos (Wikan *et al.* 2012). The adaptation of the virus was coupled with changes in the E1 glycoproteins, increasing transmissibility and driving the spread of the ECSA lineage during the outbreak.

In the Americas and Caribbean countries and territories, the first transmission was identified in late 2013 (Centers for Disease Control and Prevention 2016). By April 2015, over 1.3 million suspected

cases were reported in the United States of America, Latin American countries and the Caribbean Islands (World Health Organization 2017). The disease still mostly occurs in the Indian subcontinent, Asia, and Africa, where large outbreaks occurred in Senegal, Kenya and the Democratic Republic of Congo (DRC) in 2015, 2016 and 2019, respectively. Since the chikungunya virus emerged, it has spread to over 50 countries, making it a global pathogen (Bordi *et al.* 2015, World Health Organization 2019a). Figure 1-1 below is a map of the countries that have reported cases of chikungunya virus as of 2019.

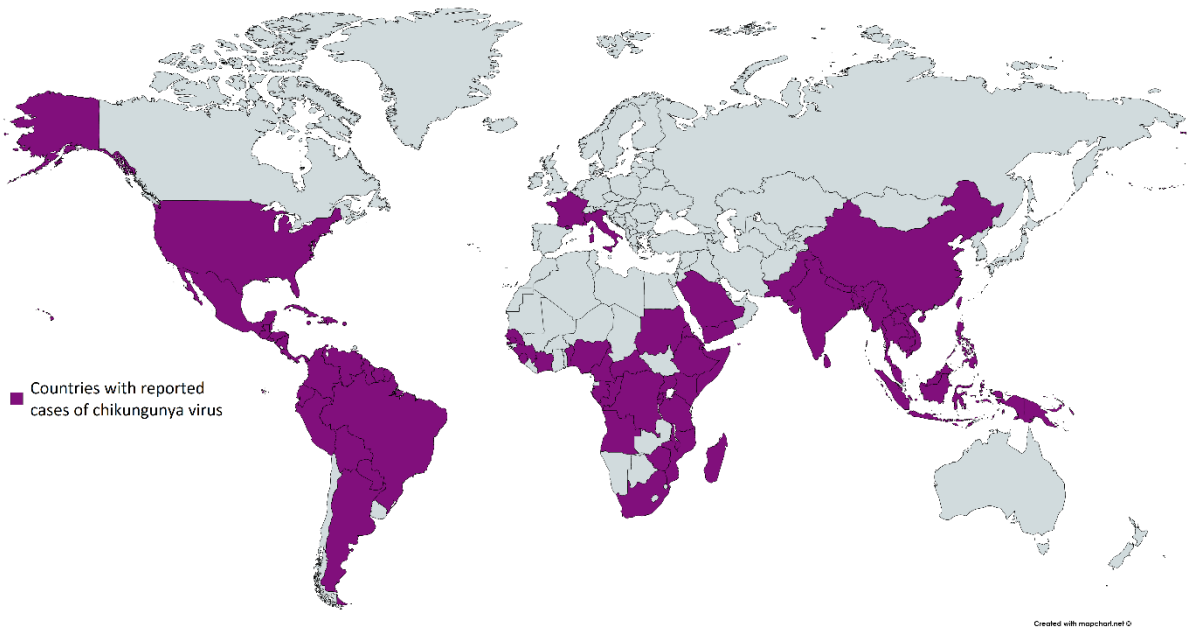

Figure 1-1: *Countries/territories with reported chikungunya virus cases as of 2019. The map shows the countries/territories where chikungunya virus cases have been reported as of 17 September 2019. The map does not include countries/territories where only imported cases have been documented. Reproduced from Centers for Disease Control and Prevention (2019b).*

The first extensive study of human cell lines infected by chikungunya virus indicated that the virus could infect various human cells (Sourisseau *et al.* 2007). Studies have also shown that the cell receptor(s) are not expressed on all human cells and are yet to be identified (Tang 2012).

Following transmission, the virus replicates in the skin and targets various cells, such as epithelial and endothelial cells, fibroblasts and macrophages derived from monocytes (Schwartz and Albert 2010). Even though an immune response can be initiated to protect skin cells, the virus can still spread rapidly into the bloodstream (Bordi *et al.* 2015). Chikungunya virus replication in the skin is limited by time and may contribute an insignificant amount to the viral load. The virus may be transported from the skin to lymphoid organs located proximally to the infection site and replicating in lymph nodes. The virus located in the lymph node utilizes the lymphatic circulatory system to travel, through the thoracic duct to the bloodstream. From here, chikungunya virus targets cells in the muscle, liver, joints and

brain (Bordi *et al.* 2015, Schwartz and Albert 2010). Chikungunya virus targets satellite cells and fibroblasts in the muscle, endothelial cells in the liver (Schwartz and Albert 2010), fibroblasts in joints, epithelial and endothelial cells in the brain.

There is no cure, vaccine or specific treatment for chikungunya virus (World Health Organization 2017). Current treatments strategies are targeted at relieving the symptoms of the virus. During chikungunya virus outbreaks, people living close to mosquito breeding sites are encouraged to minimise exposure by wearing protective clothing and applying repellents which include DEET (N, N-diethyl-3-methylbenzamide), IR3535 (3-[N-acetyl-N-butyl]-aminopropionic acid ethyl ester) or icaridin (1-piperidinecarboxylic acid, 2-(2-hydroxyethyl)-1-methylpropylester).

1.2. Morphology of Chikungunya Virus

Enveloped viruses have a viral membrane which originates from the host cell membrane during the budding stage in the virion lifecycle (Noda 2011). The viral membrane, which comprises of a lipid bilayer and envelope glycoprotein along the surface, assists with entry into the host cell and evading detection by the immune system of the host (Vu *et al.* 2017, Zhang and Dudko 2015). The envelope glycoproteins project outward as spikes and are essential for viral infectivity, playing a role in membrane binding and fusion with the host cell (Chou 2007). As a result, minor changes in the interaction of the envelope glycoproteins and receptors on the host cell membrane can have an enormous influence on the infectivity of the virion (Chou 2007). Some enveloped viruses have matrix protein along the inner surface of the membrane. The viral membrane surrounds a shell, known as the nucleocapsid, which encapsulates the viral genome and other viral proteins. The nucleocapsid shape varies depending on the virus; however, it is not always present in all enveloped viruses. The viral genome represents the deoxyribonucleic acid (DNA) or ribonucleic acid (RNA) strand(s) of the virion. Figure 1-2 is an illustration of a simple enveloped virion.

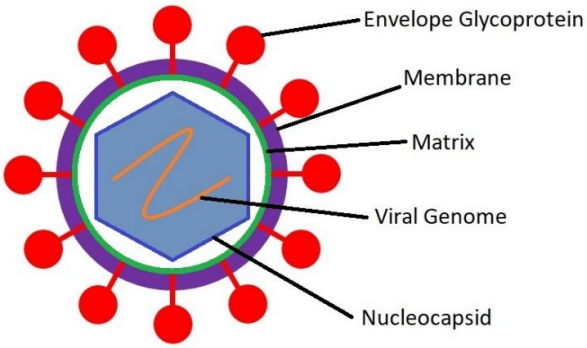

Figure 1-2: *Simple enveloped virion structure. A simple virion structure consists of the enveloped glycoproteins embedded along the surface of the membrane. The matrix protein is found on the inside the membrane which surrounds the nucleocapsid shell. The nucleocapsid protects the viral genome, which is comprised of an RNA or DNA strand(s).*

Chikungunya virions have a diameter of approximately 60-70 nm (Vu *et al.* 2017). Each virion has 80 envelope spikes, consisting of the E1 and E2 glycoproteins, in the form of a trimeric heterodimer, and are embedded in the nucleocapsid (Kuo *et al.* 2012, Sun *et al.* 2013, Van Duijl-Richter *et al.* 2015b). The E1 glycoprotein is primarily involved in membrane fusion, and E2 glycoprotein is responsible for facilitating receptor binding (Van Duijl-Richter *et al.* 2015b). The nucleocapsid, also known as the capsid, has an icosahedral shape with T = 4 quasi-icosahedral symmetry and surrounds the viral genome, a positive single-stranded RNA (Van Duijl-Richter *et al.* 2015b, Yap *et al.* 2017). The structural arrangement of a virion is illustrated in Figure 1-3.

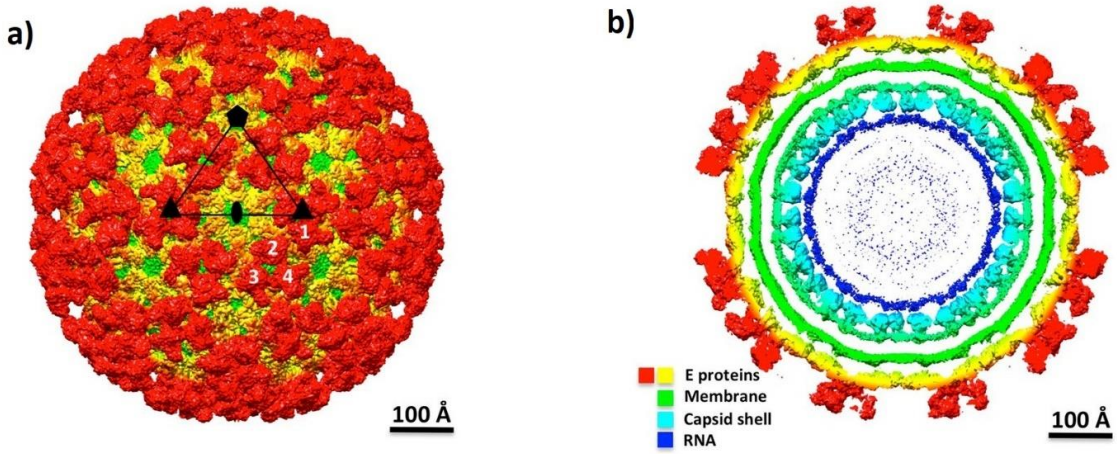

Figure 1-3: *Morphology of chikungunya virus. The (a) external and (b) internal morphology of chikungunya virus. The black triangle in (a) highlights one icosahedral unit. The structural layers are illustrated according to the colour scale in (c). Scale: 1 Angstrom (Å) = 0.1 nm. With permission from Yap et al. (2017).*

1.3. Chikungunya Virus Lifecycle

Although enveloped viruses may have differences in structure, they all follow a similar procedure to enter host cells. This procedure involves signalling to the fusion proteins to undergo conformational changes, resulting in their development as a catalyst for membrane fusion. The signal varies for enveloped viruses; for example, cell receptors influence human immunodeficiency virus (HIV) fusion with the host cell, whereas changes in pH will trigger influenza and chikungunya virus fusion proteins (Zhang and Dudko 2015). These signal-related responses form the basis from which viral entry mechanisms can be classified; the former known as fusogenic while the latter referred to as endocytotic (Chou 2007).

The fusogenic pathway, e.g. adopted by HIV, is mediated by receptor binding, which will initiate fusion of the viral and cell membrane to form a continuous membrane. Fusion of the membranes can occur immediately after receptor binding. Alternatively, the virion can be partially wrapped by the cell

membrane and requires several receptors to bind before fusion and release of the viral genome (Chou 2007). This mechanism is illustrated in Figure 1-4.

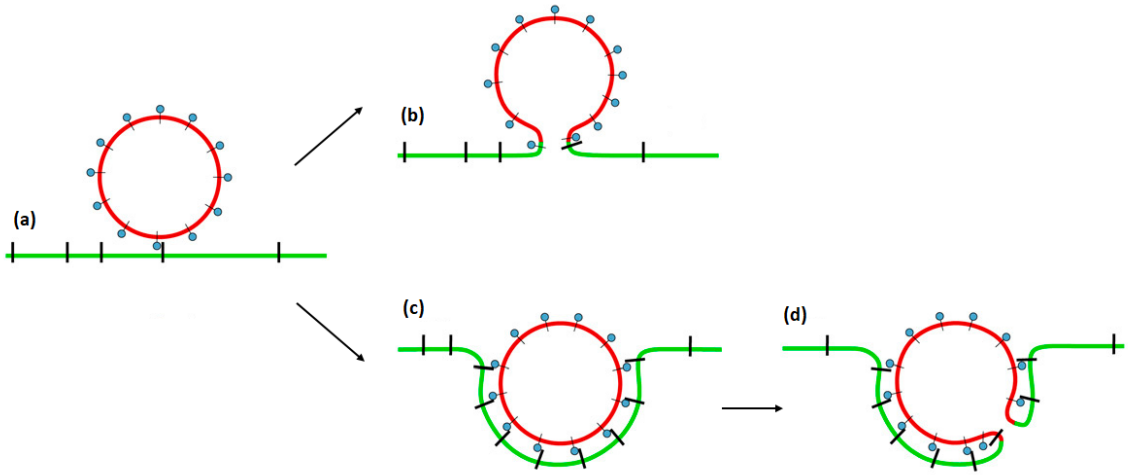

Figure 1-4: *A schematic of fusogenic viral entry. (a) A non-specific enveloped virion adheres to the cell membrane and initiating an interaction between the viral glycoproteins and host cell receptors. Fusion of the membranes can either be (b) initiated immediately after contact between the viral glycoproteins and host cell receptors or (c & d) the host cell membrane will partially wrap the virion, and then fusion will occur. Adapted with permission from Chou (2007).*

During endocytotic entry, e.g. of chikungunya virus, the virion adheres to the host cell. An interaction between the viral glycoproteins and host cell receptors occurs, and the virion is then wrapped by the host cell membrane (Chou 2007). Next, the cell membrane is pinched off, and fusion of the viral and endosomal membrane occurs. The fusion of the membranes is mediated by a low pH in the endosomal environment and will result in the release of the viral material into the host cell's cytoplasm (Chou 2007, Cross *et al.* 2001). The endocytotic mechanism is illustrated in Figure 1-5.

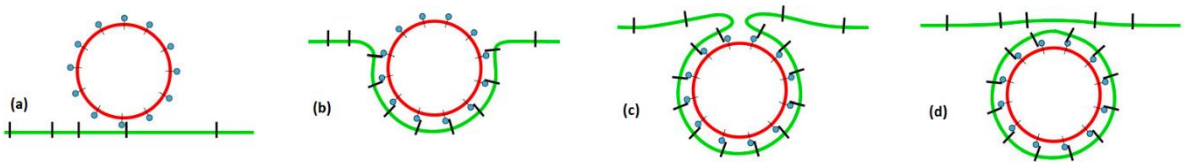

Figure 1-5: *A schematic of endocytotic viral entry. (a) A non-specific enveloped virion adhering to the cell membrane and (b) an interaction between the viral glycoproteins and host cell receptors is formed. (c) The host cell membrane then wraps and (d) internalizes the virion. Adapted with permission from Chou (2007).*

Entry into a host cell is not limited by one pathway. Some viruses, including HIV, avian leukosis retrovirus, Semliki Forest Virus and Vaccinia but not Chikungunya make use both entry mechanisms; however, this will depend on the host cell type, the type of receptors the virus will engage and whether or not these receptors induce fusion (Chou 2007).

Chikungunya virus, like other alphaviruses, uses the endocytotic mechanism to enter cells (Schwartz and Albert 2010). Chikungunya virus requires an endosomal pH of 4.5 to 5.6 with a threshold of 6.2 to induce fusion of the membranes (Kielian *et al.* 2010, Van Duijl-Richter *et al.* 2015a). Once released into the cytoplasm, the viral genome undergoes translation, processing and replication to make the sub-genomic RNA and positive-stranded RNA genome (Bordi *et al.* 2015). The viral genome is responsible for encoding the five structural precursor proteins (capsid-E3-E2-6K-E1), as well as four non-structural proteins (Sun *et al.* 2013). The non-structural proteins are responsible for virus replication, modification of proteins and protection from the immune system. The nucleocapsid core assembly involves the self-assembly of the capsid protein along with the positive-stranded RNA genome. The glycoproteins spikes are assembled in the endoplasmic reticulum (ER) and Golgi and transported to the cell membrane (Schwartz and Albert 2010). The nucleocapsid core, encapsulating the positive-stranded RNA genome, then forms a bulge on the cell membrane with the embedded spikes to form a virion, which is released from the cell. The alphavirus lifecycle is illustrated in Figure 1-6.

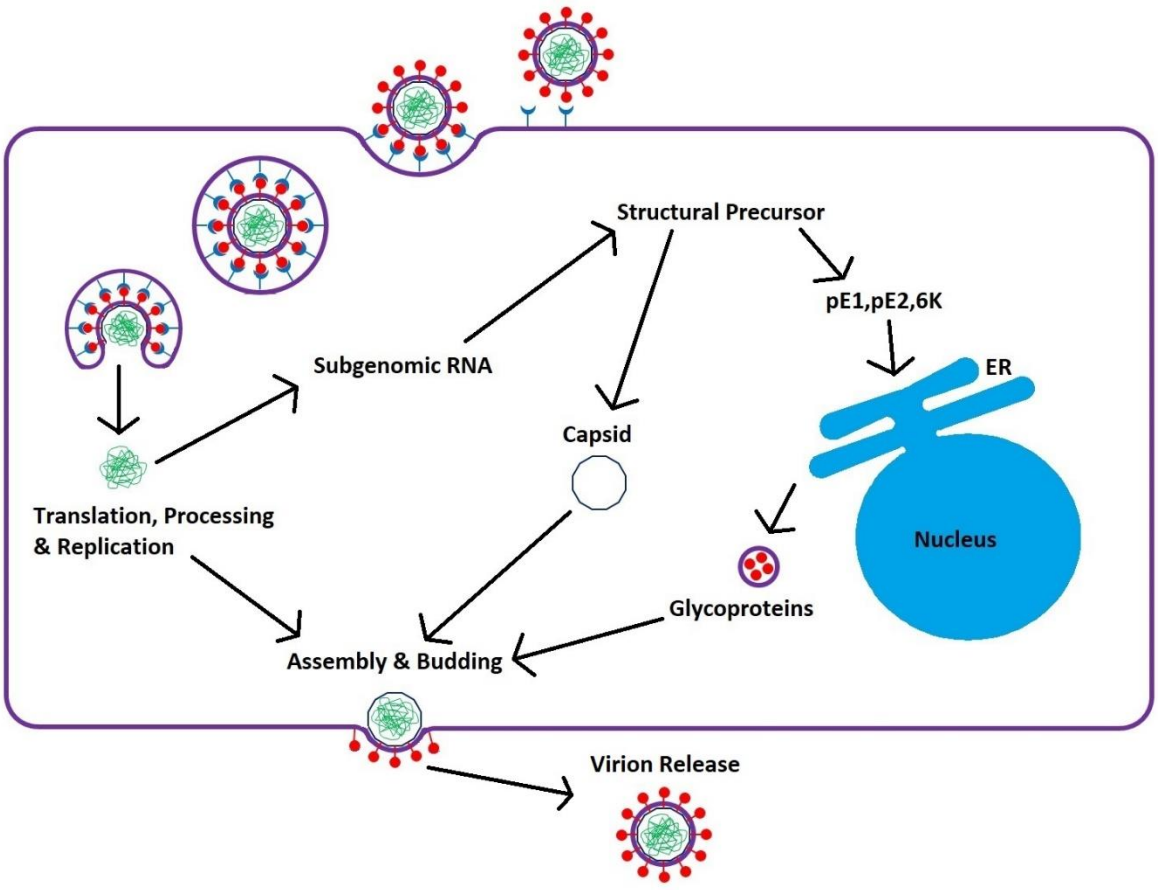

Figure 1-6: *Lifecycle of a chikungunya virion. The virion lifecycle involves docking with the host receptor protein, then wrapping of the virion to form the endosome. Lowering of pH of endosomal environment induces viral genome release. This is followed by synthesis of viral components which will then be assembled into complete viral units and bud from the host cell.*

1.4. Chikungunya Virus-Like Particles

Virus-like particles (VLP) consist of multiple subunits and can be non-enveloped or enveloped (Lua *et al.* 2014, Zeltins 2013). VLPs have an identical or similar morphology to the wild-type (WT) virion; however, lack the viral genome (Lua *et al.* 2014, Noranate *et al.* 2014). As a result, the VLPs are not infectious, but they mimic the conformational changes of the WT virion (Noranate *et al.* 2014). VLPs have similar immunogenic and antigenic properties as their native virion, which allow them to have various applications, such as in vaccines, gene therapy tools and biotechnology (Zeltins 2013). Biotechnology applications involve employing methodologies from various disciplines to develop nanomaterials composed of different viruses and VLPs (Zeltins 2013).

The five structural precursor proteins (capsid-E3-E2-6K-E1) of chikungunya virus are used to create chikungunya VLPs (Sun *et al.* 2013). Figure 1-7 is an illustration of the morphology of chikungunya virion compared to a chikungunya VLP.

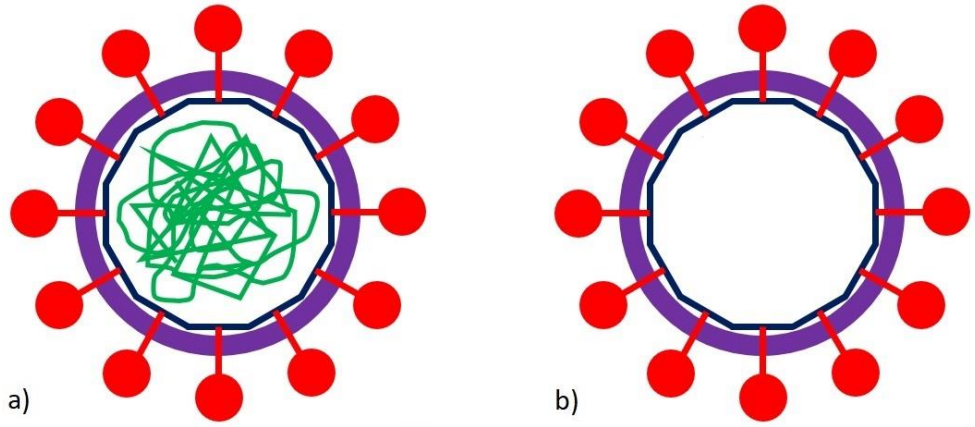

Figure 1-7: *Morphology of a chikungunya virion vs. a chikungunya VLP. An illustration of the general structure of a) a chikungunya virion and b) a chikungunya VLP. VLPs do not contain the viral genome.*

1.5. Morphology of the Human Cell Membrane

The cell membrane, also known as the plasma membrane, is a semi-permeable barrier that protects the inner cell from the outside environment (Goni 2014, Nicolson 2016). The cell membrane consists of the phospholipid bilayer. The phospholipids are amphipathic and comprise of a hydrophilic phosphate head and hydrophobic tail. The hydrophobic tails face each other, whereas the hydrophilic heads face the exterior space. The cell membrane includes membrane proteins, known as integral and peripheral proteins. Channel protein is a type of integral protein which acts as a gateway for transporting substances. Other features of the cell membrane include glycoproteins, globular proteins, carbohydrates, cholesterol and alpha-helix proteins. Figure 1-8 illustrates a fluid-mosaic model of the cell membrane structure.

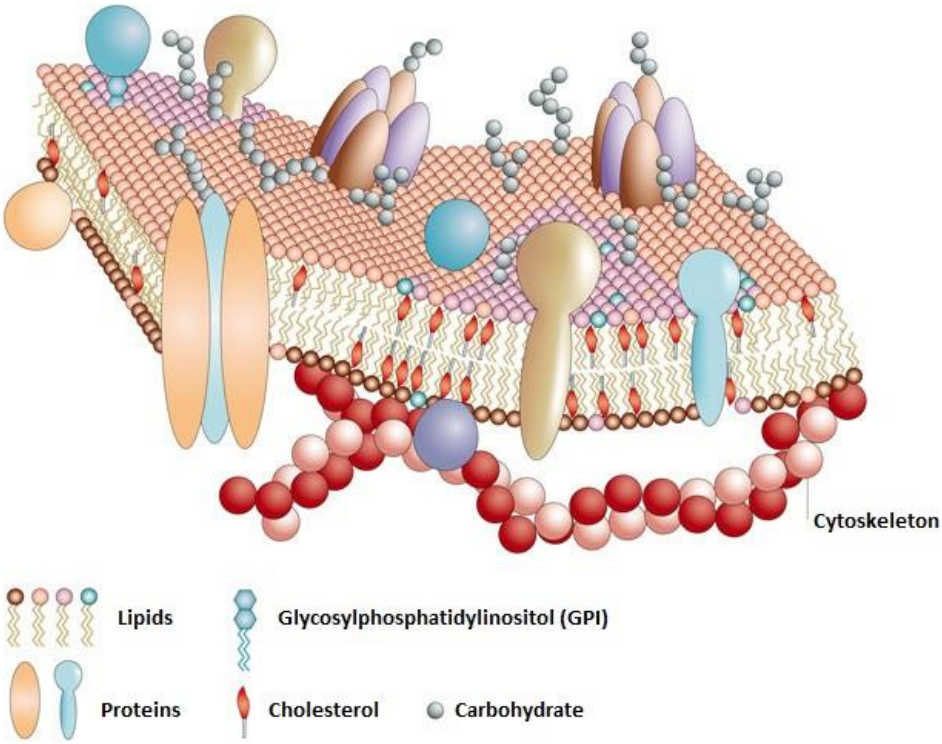

Figure 1-8: *Fluid mosaic model of the cell membrane. The fluid mosaic model includes a phospholipid bilayer, carbohydrates, cholesterols and various other membrane proteins. With permission from Pietzsch (2004).*

1.6. Mechanical Virology

The mechanical properties of virions can be analysed using atomic force microscopy (AFM). AFM makes use of a cantilever which indents the virion and uses the deformation to determine the spring stiffness of the virion. Mechanical virology studies the relationship between the mechanical and material properties of the virion capsid and their impact on the morphological changes throughout the virion lifecycle (Marchetti *et al.* 2016)

Virions may undergo conformational changes during the process of maturation in preparation for infection of the host cell. For some virions, like the Bacteriophage HK97 virion, these conformational changes involve large structural adjustments, resulting in an increased infectivity (Veesler and Johnson 2012). Bacteriophage HK97 virions transitions from the Prohead I form (P-I) to the Prohead II form (P-II), when the N-terminal polypeptide, known as the Δ-domain, is cleaved from the capsid protein subunits, gp5 (Roos *et al.* 2012). The protease, gp4, is responsible for cleavage of the Δ-domain, which is assumed to be responsible for capsid assembly (Roos *et al.* 2012). Nanoindentation of the Prohead I and II forms using AFM indicates that the transition of the virion increases the spring constant from 0.018 N/m to 0.12 N/m, resulting in a stiffer virion (Roos *et al.* 2012). The Prohead II form expands

from a diameter of approximately 50nm to a structurally stable capsid of approximately 60 nm, known as the Expansion Intermediate (EI). EI formation causes the formation of cross-linked covalent bonds that lead to expansion of the virion to the balloon form, then the icosahedral shaped Head II (H-II) form. The expansion of the bacteriophage from the P-II form to the H-II form is associated with an increase of the Young's modulus from 0.3 to 1.0 GPa and an increase in breaking force from 0.56 to 0.9 nN. This indicates that maturation of the virion is linked to the mechanical stabilization of the capsid, necessary for the protection of the viral genome and protection from the environment to ensure the virion reaches the target cell (Marchetti *et al.* 2016, Roos *et al.* 2012). An illustration of the capsid expansion is shown in Figure 1-9.

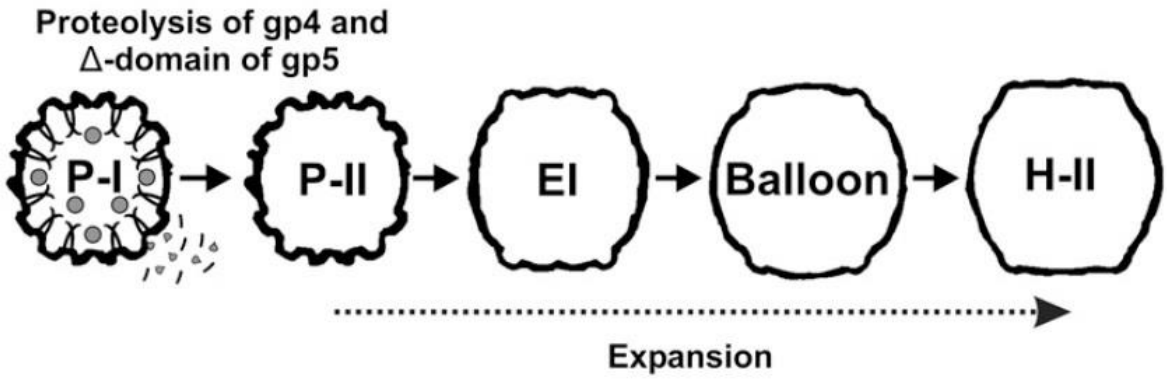

Figure 1-9: *The expansion of the Bacteriophage HK97 virion during maturation. The Δ-domain, which is responsible for capsid assembly, is cleaved from the Prohead I form to transition into the Prohead II form. The capsid undergoes further expansion to reach the mechanically stable Head II form. Adapted with permission from Roos et al. (2012).*

The interaction between HIV viral Gag protein and the envelope protein may play a role during fusion of the host cell and virus (Gibbons and Klug 2007, Murakami *et al.* 2004, Roos *et al.* 2012, Wyma *et al.* 2004). It has been found that truncation of the cytoplasmic tail (CT) of the envelope protein in the mature virus reduces its fusion efficiency while removing the CT of the envelope protein in immature virions improves fusion with the host cell. This suggests that the cleavage of the CT causes conformational changes in the Gag protein, which activates fusion competence (Murakami *et al.* 2004, Wyma *et al.* 2004). The reorganisation of the internal structures of HIV during maturation is associated with a change in stiffness of the virus (Gibbons and Klug 2007, Kol *et al.* 2007). The immature virus is more than 14-fold stiffer than the mature virus; however, the immature virus with truncated CT has a similar stiffness to the mature virus. An investigation can be performed to determine the influence stiffness has on entry ability by isolating the virus' stiffness-mediating and entry-inducing domains (Pang *et al.* 2013). By fixing the entry-inducing domains and varying the stiffness-mediated domains

in an immature particle, the entry ability of the virus is tested. It is found that with increasing stiffness, the immature virus demonstrates more significant impairments in entry ability, confirming the link between stiffness and entry ability.

Influenza virus, like chikungunya virus, enters the host using the endocytotic mechanism (Hoornweg *et al.* 2016). Nanoindentation experiments of Influenza virus using AFM indicates the virus removes its coating in a two-step process, to release the viral genome (Greber 2014, Li *et al.* 2014). Experiments conducted on influenza type A indicate that the two-step uncoating relates to early and late endosomal environments with corresponding pH values. Each step is pH dependant and is associated with a softening of the virus (Greber 2014, Li *et al.* 2014, Marchetti *et al.* 2016). The early endosomal environment has pH 7.4 - 6.0 and is indicated by the softening of the envelope glycoproteins, hemagglutinin (HA). The late endosomal environment has pH 6.0 - 5.5 and is associated with the disassembly of the matrix protein (M1) lipid layer and its dissociation from the lipid bilayer. The pH of the first step initiates the morphological changes linked to the infection process and the pH of the second step results in the irreversible softening of the virion and morphological changes, necessary for the release of the viral genome. The two-step uncoating process is illustrated in Figure 1-10.

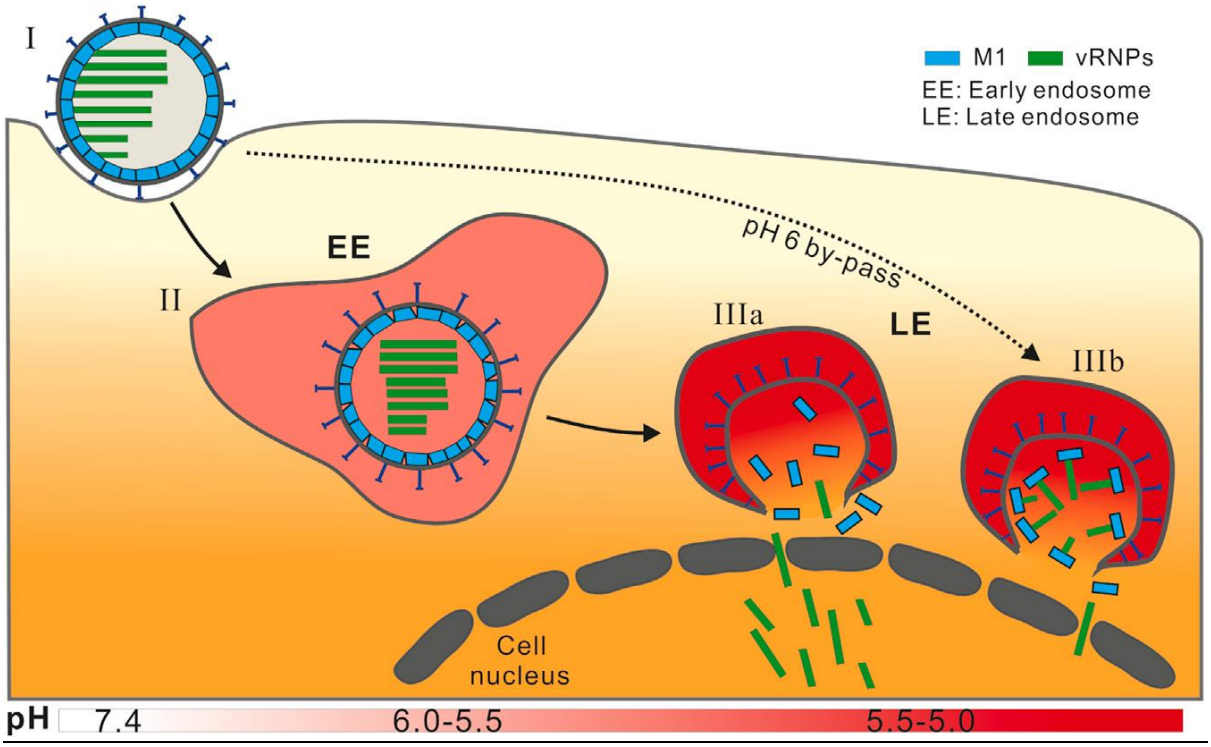

Figure 1-10: *Two-step uncoating of the influenza virus. In the early endosomal (EE) environment, the envelope glycoproteins are softened. This was followed by the late endosomal (LE) environment, which was indicated by disassembly of the M1 layer its disassociation from the lipid layer in order to release the viral genome. With permission from Li et al. (2014).*

1.6.1. Mechanical Assessment of Virions using Atomic Force Microscopy

Atomic force microscopy (AFM) is used for imaging and performing nanoindentation tests. The sample is immobilized on the substrate fixated on the piezoelectric scanner, known as the piezo. The piezo can move the sample in the x, y, and z directions. A nanometre-sharp tip attached to the free end of a flexible cantilever scans over the sample. Reflection of a laser beam off the cantilever is directed to the quadrant photodiode. As the cantilever scans over the sample, it deflects in the z-direction following the surface topography of the sample. This causes a change in the angle of the laser beam detected on the photodiode. The photodiode detects the light intensity of the laser beam and converts it to a voltage signal. Figure 1-11 is an illustration of a sample scanned using AFM.

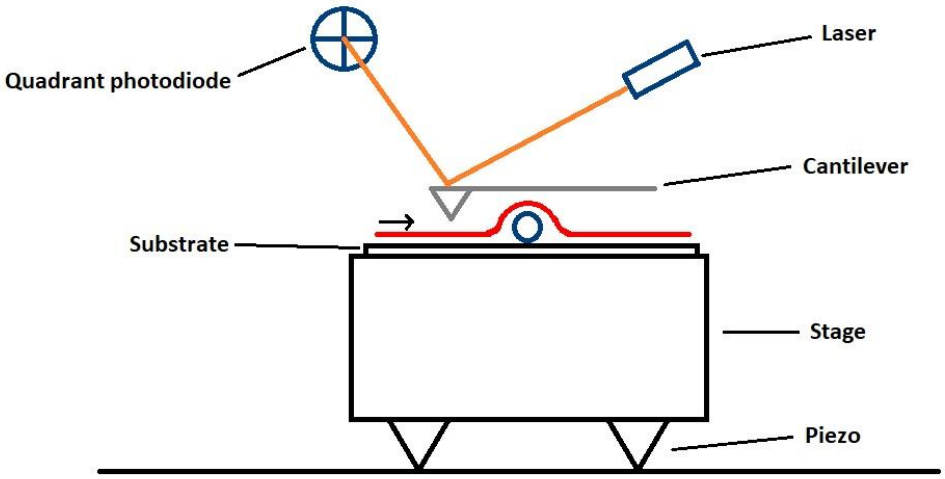

Figure 1-11*: Simple AFM setup. The red line indicates the path travelled by the cantilever, and the arrow indicates the direction. As the cantilever deflects in the z-axis, it moves along the topography of the sample, and these changes are recorded on the photodiode.*

A topography map of the sample is generated using the z-direction heights, as seen in Figure 1-12. The bottom morphology of the sample is not discernible, as shown in Figure 1-11 and Figure 1-12.

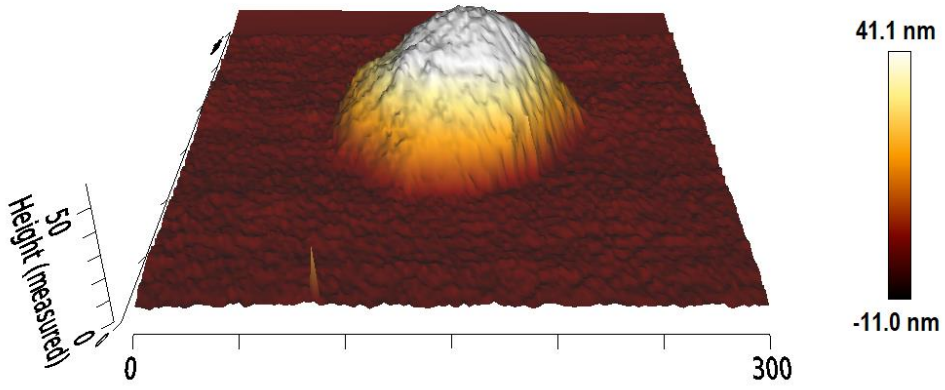

Figure 1-12: *Topography map of an enveloped virion. The virion imaged is spherically shaped. The units for all axes are nm.*

The nanoindentation test takes place after imaging and involves locating a point on the sample, such as the centre, and applying a force. As the sample deforms, the force-displacement curves are recorded. The force-displacement curves give information on the elastic properties of the sample and plastic deformation, which may occur. Some force-displacement curves show a peak then sudden drop in force which indicates the breaking point of the sample.

AFM can operate in various modes, such as contact, jumping/pulsed and dynamic mode. Contact mode is where the tip of the cantilever is in direct contact with the substrate and sample, as it scans in the x and y direction, illustrated in Figure 1-11. Jumping/pulsed mode combines features from contact and dynamic mode, shown in Figure 1-13.

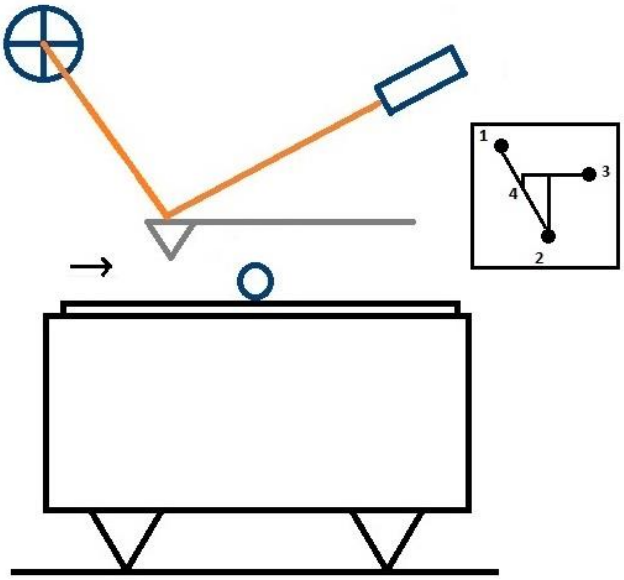

Figure 1-13: *Imaging using jumping/pulsed mode. The arrow indicates the direction the cantilever scans the sample. The inset is the force vs extension curve measured at every pixel. Point 1 is the maximum height of the cantilever before approaching the sample. Point 2 is the maximum deflection point of the cantilever. Point 3 is the maximum distance between the sample and the tip. Point 4 is the point of contact between the tip and sample.*

Dynamic mode, also known as tapping mode, the cantilever is in intermittent contact with the surface and involves oscillating the cantilever with a user-specified fixed amplitude at a high frequency or close to its resonant frequency. Figure 1-14 is an illustration of imaging using dynamic mode.

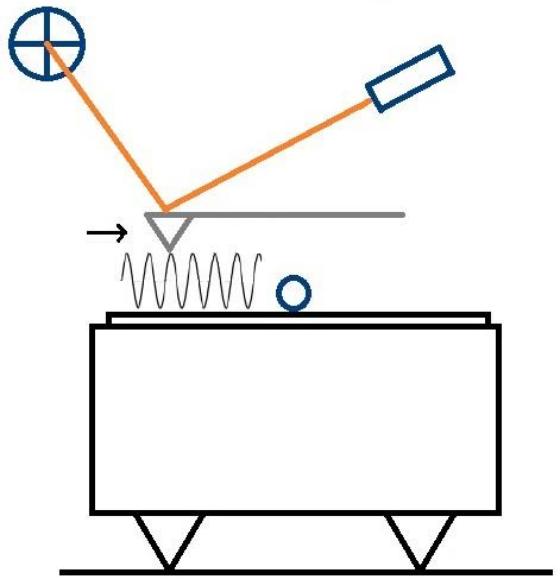

Figure 1-14: *Imaging using dynamic mode. The cantilever scans over the sample in the direction shown by the arrow and oscillates at a user-specified fixed amplitude.*

The disadvantages of contact mode are the force applied, and lateral movement introduce friction between the cantilever and sample, which may result in damage or movement of the sample. Also, the set point of the force is user-specified and was related to the position of the cantilever on the photodiode as it deflects and is not an indication of a constant force applied during imaging. Jumping/pulsed mode is beneficial because it minimizes the shear forces as the cantilever scans and is in contact with the surface. The mechanical properties of samples can be determined using this mode because the forces applied are controlled precisely, and force-displacement curves can be generated for each point on the image. However, the image rate is low because of the time spend on each operating cycle. Dynamic or tapping mode can also be used to determine the mechanical properties of the sample; however, this mode is based on damping, which reduces the quality factor of the system. Damping makes the system less sensitive; therefore, the cantilever may not reach the surface in every step. Nevertheless, the reduction in the degree of freedom of the amplitude regarding the dynamic mode, limits the force applied and renders better quality images. For this project, imaging is done using dynamic mode, and nanoindentation experiments are done using jumping/pulsed mode (Baró and Reifenberger 2012).

For all experiments, it was essential that the cantilever tip and substrate are clean. Impurities may taint the sample, making it difficult to distinguish between the impurities and the target objects for imaging and nanoindentation. The impurities may also cause damage to the apex of the tip or attach

to the tip causing a double tip effect. An example of this is shown in Figure 1-15. Typical substrates used are silicon, glass. For this project, glass substrate was used.

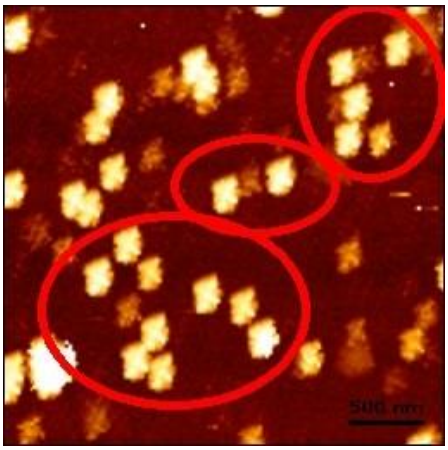

Figure 1-15: *Cantilever artefacts. The image is taken of a chikungunya virus sample. The particles enclosed in red circles all have a similar, irregular shape which may be an indicator of impurities attached to the tip.*

1.7. Image-based 3D Modelling of Viruses

Three-dimensional (3D) cryogenic electron microscopy (cryo-EM) can be used to visualise and study the structures of virions at near-atomic resolution (Sirohi *et al.* 2016). Katz *et al.* (2014) studied the morphology of influenza type B virions, providing insight into the importance of the relationship of the matrix protein (M1) with both the ribonucleoprotein (RNP) and envelope glycoprotein. The M1 layer may be responsible for organising the structure of the whole virion. The study also quantified the number and distribution of the envelope glycoproteins, hemagglutinin (HA) and neuraminidase (NA), on a typical 130 nm diameter type B virion. The geometry of a typical influenza type B virion is shown in Figure 1-16.

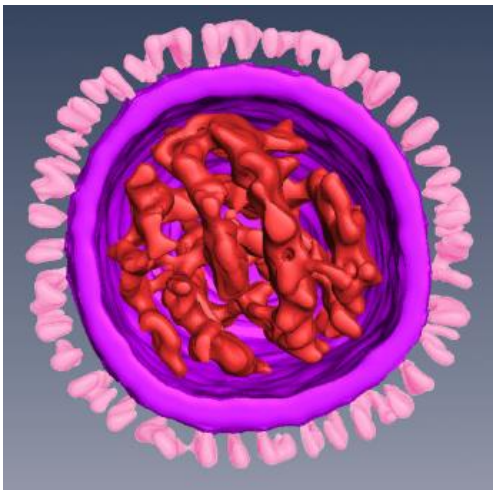

Figure 1-16: *Reconstruction of a typical influenza type B virion. A typical type B virion has a diameter of 130 nm. The RNP (red) is surrounded by the M1 layer (purple). The envelope glycoproteins (HA and NA), indicated in pink, are arranged on the surface of the M1 layer. With permission from Katz et al. (2014).*

Chen *et al.* (2017) studied the structure of isometric mutant bacteriophage T4 capsids at a resolution of 3.3 Å. The capsid assembly precursor of a bacteriophage T4 virion, known as the prohead, has four proteins on the outer surface. The proteins include the capsid proteins, gp23 and gp24, the small outer capsid (Soc) protein and the highly immunogenic outer capsid (Hoc) protein. Mutations in these proteins can produce changes in the length of the virion, resulting in prolate (Figure 1-17 (a)) and icosahedral (Figure 1-17 (b)) capsids. Analysis of the mutant bacteriophage T4 capsids has shed light on the assembly of other icosahedral virions with a specified T number.

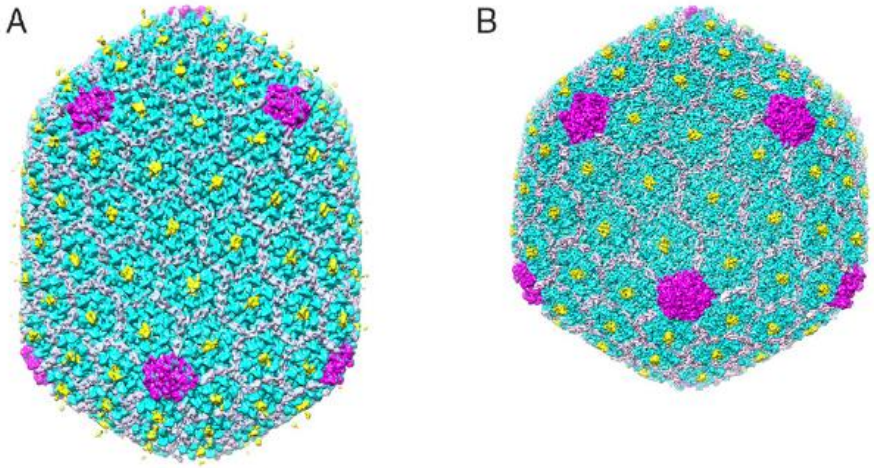

Figure 1-17: *Reconstruction of mutant bacteriophage T4 capsids. Mutant bacteriophage T4 wild-type (WT) a) prolate capsid and b) isometric capsid geometries a presented at 3.3 Å resolution. The prolate capsid is characterised by T_{ends} = 13 for the icosahedral ends and T_{mid} = 20 for the elongated section. The icosahedral capsid is characterised by T = 13 and has a diameter of 86 nm. The different colours represent the proteins on the outer surface of the capsids. Gp23*[1], gp24*[2], Hoc, and Soc are coloured blue, magenta, yellow, and white, respectively. With permission from Chen et al. (2017).*

Kruse (2017) also developed a 3D geometric model using 2D images of a mature HIV virion with the capsid isolated from the virion shell. The 3D geometric model was further modified by occluding the capsid and optimising the virion shell to ensure it is continuous. The fragmented virion shell is a result of the limitations of the electron microscopy (EM) sample stage and its inability to image through a full 180° range (Kruse 2017). Processing the fragmented 3D geometric model using Simpleware ScanIP software rendered a continuous model that can be used in finite element simulations, as seen in Figure 1-18.

[1] Mutant gp23
[2] Mutant gp24

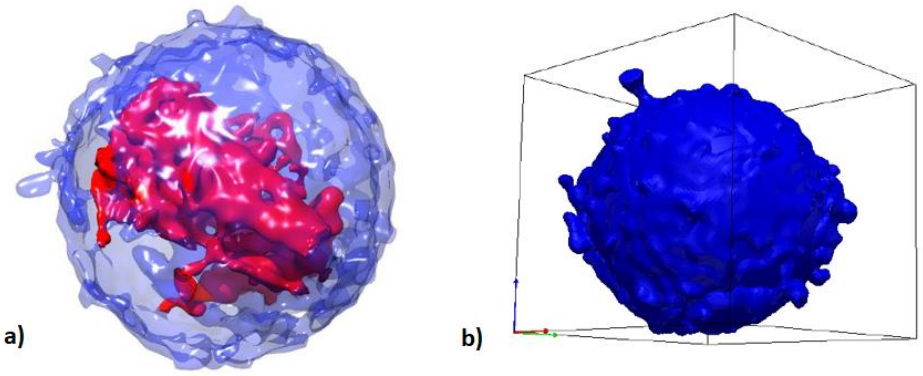

Figure 1-18: *A reconstructed model of an HIV virion. a) The capsid is illustrated in red and the virion shell in blue. The image was reconstructed using UCSF Chimera. b) The reconstructed continuous 3D geometric model was created using Simpleware ScanIP. With permission from Kruse (2017).*

Sun *et al.* (2013) and Yap *et al.* (2017) reconstructed a 3D model of a chikungunya VLP using a cryo-EM map with a resolution of 5.3 Å and 6.8 Å respectively. Features such as the E1 and E2 glycoproteins, membrane, nucleocapsid, transmembrane (TM) helixes and asymmetric icosahedral units were discernible from the reconstruction. The structure of a chikungunya VLP from the reconstruction is shown in Figure 1-19.

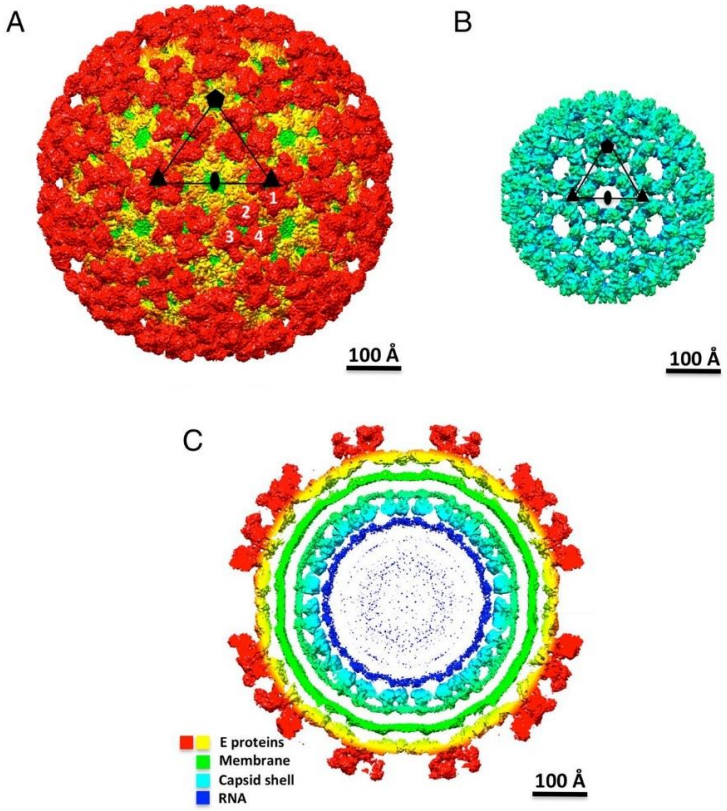

Figure 1-19: *Reconstruction of chikungunya VLP. The image illustrates the reconstructed a) VLP and b) nucleocapsid and c) cross-section of the VLP. The envelope glycoproteins are visible on the surface of the VLP. The black triangle in (a) highlights one icosahedral unit. The structural layers are illustrated according to the colour scale in (c). Scale: 1 Angstrom (Å) = 0.1 nm. With permission from Yap et al. (2017).*

1.8. Finite Element Modelling of Viruses

The uniformity and predictability of empty capsid shells make them the optimal option for studying the physical properties of viruses in finite element models (Roos *et al.* 2010). The mechanical properties of viral capsids can be studied by simulating AFM nanoindentation experiments and calibrating models to experimental data.

A simplified 2D or 3D geometries of virions can be used in finite element analysis in mechanical and mechanobiological simulations (Kol *et al.* 2006). An example of this can be seen in the constructed geometries of Murine Leukaemia Virus, which consists of two hollow spheres with varying thicknesses in Figure 1-20.

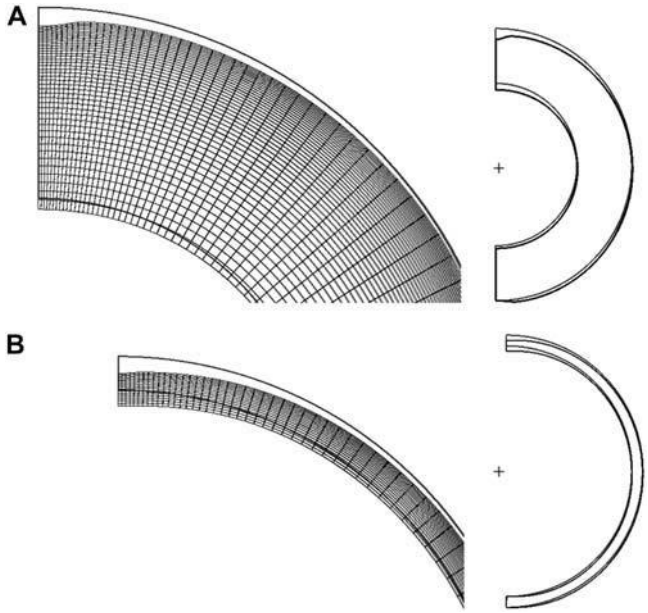

Figure 1-20: *Finite element simulation for indentation of immature and mature virions. Finite element simulation for indentation of (a) immature and (b) mature virions, both with an outside diameter of 50 nm. The immature virions have a shell thickness of 20 nm while the mature virions have a shell thickness of 4 nm. With permission from Kol et al. (2006).*

Michel *et al.* (2006) and Gibbons and Klug (2007) both developed simplified geometries for cowpea chlorotic mottle virus (CCMV) for finite element simulations and found that these offered insights into the structural properties of the virus and the effect model parameters have on the virus. These insights have helped validate and enable comparisons to AFM experiments.

Ahadi *et al.* (2009) studied the indentation behaviour of empty viral capsids belonging to various viruses with two morphologies, spherical and icosahedral. The viruses studied are Parvovirus minute virus of mice (MVM), CCMV, bacteriophage λ, bacteriophage G and Mimivirus, and the viral capsids are modelled as nonlinear Hookean elastic thin shells. The Young's modulus is determined by

calibrating the indentation curves from the simulation to experimental data. The indentation behaviour of spherical capsids displayed linear behaviour; however, capsids with a prominent icosahedral shaped displayed nonlinear behaviour. The indentation behaviour of bacteriophage λ viral capsids is illustrated in Figure 1-21.

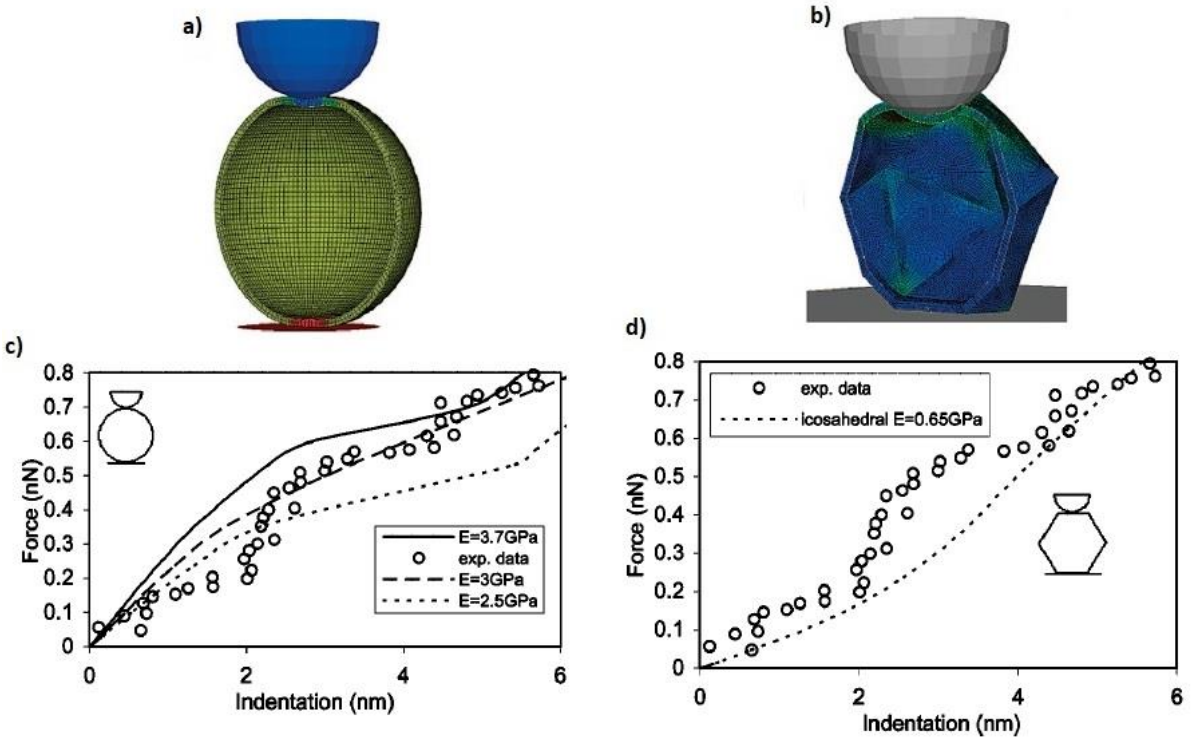

Figure 1-21: *Indentation of spherical and icosahedral shaped Bacteriophage λ capsid shells using finite element simulation. The finite element models setup of a) a spherical shaped Bacteriophage λ capsid and b) icosahedral shaped Bacteriophage λ capsid. The image includes the comparison of the force-indentation curves of the experimental data and finite element simulation results with various Young's moduli for the c) spherical shaped and d) icosahedral shaped capsid. With permission from Ahadi et al. (2009).*

Roos *et al.* (2010) studied the orientation-dependent indentation behaviour of Hepatitis B virus (HBV) capsids. The virus has an icosahedral shape and approximately 30 nm in diameter. The HBV capsids were modelled with 3D topographical detail. The capsids were indented with forces below 0.8 nN and the deformation experienced by the capsid was modelled by finite-deformation continuum hyper-elasticity with a neo-Hookean constitutive law. The Young's modulus (E) of the capsids was 0.26 GPa. The disparities in capsid thickness and interaction between the cantilever tip and 3D topographical detail attributed to the nonlinear indentation behaviour of the capsid. The 3D topographical detail on the virion characterised the indentation behaviour of Hepatitis B capsids more accurately than thin shell icosahedral-shaped models. The indentation curves of the capsids are illustrated in Figure 1-22.

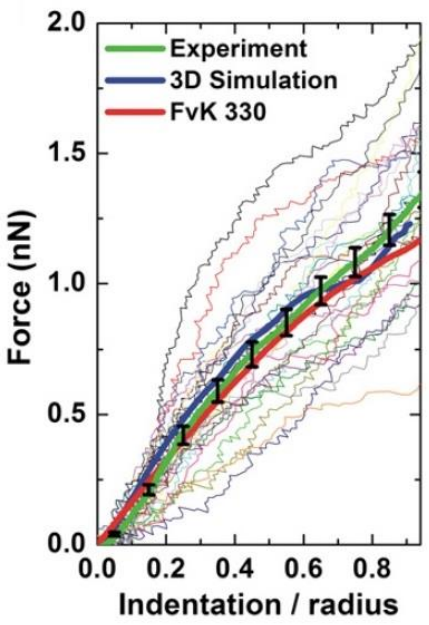

Figure 1-22: *Comparison of force-indentation curves of Hepatitis B. The graph represents indentation curves from experimental data (thin lines), the average of these curves (thick green line) with error bars (SEM). The graph also represents the indentation behaviour of 3D topographically detailed models (thick blue line) and thin shell models with FvK 330 (thick red line). The capsids are indented along the T = 4 symmetry axis. With permission from Roos et al. (2010).*

1.9. Problem Identification and Limitations of Past Research

There are problems that have been identified for the investigation of mechanobiological interactions between virions and host cells involved in the infection process. These problems include:

- There has been limited research on the mechanical assessment of chikungunya virus throughout its lifecycle, particularly the virions interaction with the host cell membrane.
- Mechanobiology has shown that the mechanical and morphological properties of viruses may play a role in viral entry and progression.
- Computational modelling of infectious viruses has focussed on simplified 2D or 3D models; however, topographically detailed models more accurately characterise the behaviour of viruses.

1.10. Aim and Objectives

Millions of people have been infected globally, and many more will be infected with the Chikungunya virus in future years. There is no cure or vaccination to date and current treatment strategies involve treatment of the symptoms. Based on the limitation of past research, this project therefore aimed to study experimentally and computationally the mechanical properties and morphology of chikungunya

as an enveloped virus to enable investigations of mechanobiological interactions between virions and host cells involved in the infection process.

The objectives derived for the project were:

1. To study the mechanical properties of chikungunya virions and how these are affected by the environment.

   The hypothesis related to this objective was that a decrease in pH in the endosomal environment would result in increased stiffness of the chikungunya virions.
2. To develop 3D computational geometries and finite element models of chikungunya virions that can be used for computational investigations of the mechanics of chikungunya virions, and more generally enveloped virions, and their interactions with host cells.

2. Mechanical Assessment of Chikungunya Virus-Like Particles in different Endosomal Environments

2.1. Introduction

Studying the mechanical properties of virions is essential in understanding their structure and function. The stiffness of virions has been found to change throughout the virion lifecycle and stiffness is linked to the infectivity. Atomic force microscopy (AFM) was used to perform nanoindentation experiments of virions to understand their mechanical properties. AFM nanoindentation experiments allow for single-particle analysis and determining the spring constant of virions. AFM can also determine the deformation and force at which failure occurs.

2.2. Materials and Methods

The mechanical assessments using AFM were performed at the Zernike Institute of the University of Groningen. This project aims to study the mechanical properties of the chikungunya virus in the endosomal environment before and after acidification. Acidification of the endosomal environment is necessary to create conditions that prepare the virions for fusion. This section covers the sample preparation, experimental procedure, data and statistical analysis, results obtained and discussion of the results.

2.2.1. Virus Material and Preparation

The chikungunya virus S27-African prototype (Van Duijl-Richter *et al.* 2015a) provided by S. Günther from the Bernhard-Nocht-Institute for Tropical Medicine (Hamburg, Germany) was used. This strain was isolated in Tanzania in 1953, and Vero-WHO cells were used to cultivate seed stocks (Van Duijl-Richter *et al.* 2015a). A confluent monolayer of Vero-WHO cells was infected with chikungunya virus strain S27 at a multiplicity of infection of 0.01. The cell supernatant was harvested 48 hours post infection and spun by low-speed centrifuge to remove it from the cell debris. To use the virions outside a biosafety level 3 environment, they were inactivated using UV radiation for 24 minutes. The virions were purified on a continuous sucrose gradient, frozen in liquid nitrogen and stored at -80°C with 25 µl of the sample in each test tube. An estimate of the structural breakdown of chikungunya virions is shown in Figure 2-1.

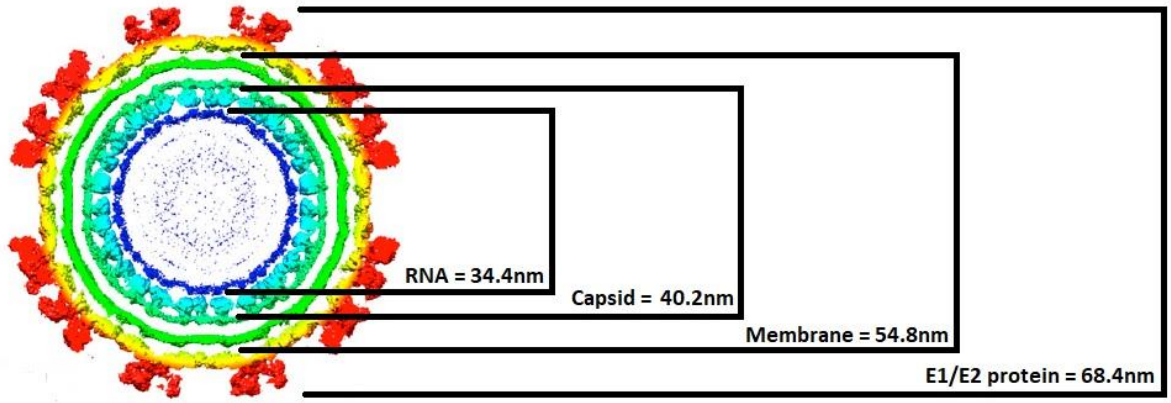

Figure 2-1: *The structural breakdown of chikungunya virus. An estimate of the structure of the virion was determined by measuring EM data of chikungunya virions. The image indicates the diameter of the RNA, capsid, membrane and whole virion (E1/E2 protein). Adapted with permission from Yap et al. (2017).*

Before each experiment, the sample was thawed at room temperature. A PD MiniTrap G-25 column, following gravity protocol, was used to remove the sucrose and reduce the concentration of the virions to prevent crowding of the virions during the nanoindentation experiment. The buffer used was phosphate-buffered saline (PBS) with ethylenediaminetetraacetic acid (EDTA). The EDTA was responsible for chelating calcium found in the sample.

The top and bottom caps of the column were removed, and the storage solution was allowed to flow through. The column was filled twice with PBS (approximately 8 ml) which flowed through and was discarded. The 25 µl chikungunya virion sample was added to the centre of the column followed by 475 µl of PBS. The sample and buffer were allowed to completely enter the column bed before the excess buffer was discarded. A test tube was placed under the column to collect the sample. Forty (40) µl of the eluent (PBS) was poured, and the eluate was collected. Figure 2-2 illustrates the elution process.

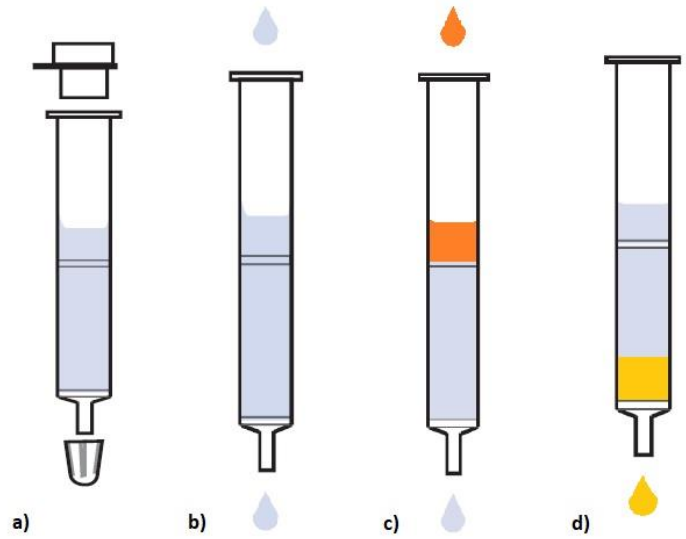

Figure 2-2: *Illustration of the elution process followed to remove sucrose and calcium from the sample. In a) the PD MiniTrap G-25 column was prepared by removing the top and bottom cap. This was followed by b) column equilibration where +/-8 ml of PBS was allowed to flow through. In c) sample application, the sample (shown in orange) was added the column followed by the 475 µl of PBS. In d) the eluate (shown in beige) was collected and used for testing.*

2.2.2. Hydrophobic Glass Coverslip and Sample Preparations

Hydrophobic coated glass coverslips were the substrate used for the experiments. The coverslips need to have a hydrophobic coating to ensure the virus material adheres to the substrate. The hydrophobic glass coverslips were prepared in the fume hood. The coverslips were rinsed with 96% ethanol and wiped with lint free tissue to remove all dust particles. They were placed in a glass holder using tweezers and stored in a 250 ml glass box in the fume hood. Twenty-five (25) g of Potassium Hydroxide (KOH) was slowly poured in 25 ml MilliQ water while stirring continuously. The solution was left to cool in the fume hood before adding 96% ethanol to make a total volume of 250 ml. The final concentration of KOH in the solution was 0.1 g/ml. The glass box with the coverslips was filled with the KOH solution, sealed with a lid and left to incubate overnight (approximately 15 hours) in the fume hood (Roos 2011, Snijder *et al.* 2012).

The lid was removed, and the glass holder was taken out the KOH solution. The KOH solution was discarded, and the glass box and coverslips were thoroughly rinsed with MilliQ water. This was done by first rinsing the lid, filling the glass box including the glass holder and coverslips with MilliQ water, removing the glass holder including the coverslips from the glass box and rinsing the glass box. This step was repeated at least twice. The coverslips were blow dried individually using argon gas, ensuring that once the centre of the coverslip was dry, it remains dry while changing the blow direction. The

glass coverslips, including the glass holder, were placed in the glass box with the lid partially closed and left to dry overnight in the fume hood (Roos 2011, Snijder *et al.* 2012).

Should the glass coverslips, holder and glass box not be dry, they were left again to dry overnight. This step was repeated until the coverslips, holder and glass box were dry.

One (1) ml of Hexamethyldisilazane (HMDS) was added in the glass box including the glass holder and coverslips, covered with the lid and sealed with parafilm to prevent air from coming in or going out the glass box. The addition of HDMS was responsible for created a hydrophobic surface repellent on the glass coverslips which repels dust and water. The HDMS also results in the virus material adhering to the coverslips without compromising the mechanical integrity of the virus. The glass box, including the glass holder and coverslips, were left to incubate overnight (approximately 15 hours) in the fume hood (Roos 2011, Snijder *et al.* 2012).

The parafilm seal was removed, the lid partially opened, and the glass box was left to incubate in the fume hood for 3 hours. The glass box was then closed, and the coverslips were ready for use.

The coverslip was placed in the AFM sample holder, and 10 µl of the virus sample was placed in the centre of the coverslip and allowed to incubate for 15 minutes (as seen in Figure 2-3). Once the incubation period has ended, 500 µl of the buffer (see 0

pH Adjustment) was added around the sample.

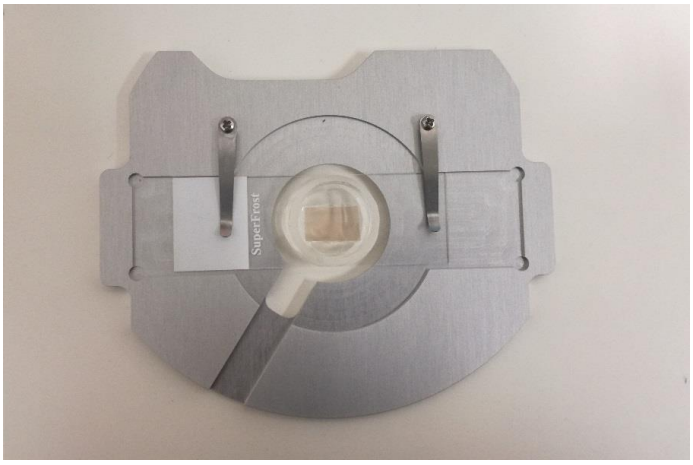

Figure 2-3: *AFM sample holder with the sample. The AFM sample holder secures the substrate, ensuring there was no movement during the nanoindentation experiments.*

2.2.3. pH Adjustment

The virions were tested in two environments, each representing endosomal environments:

1. a neutral extracellular environment with a pH that does not promote fusion of the virions;
2. acidic endosomal environment with a pH that promotes fusion of the virions.

The nanoindentation tests were divided into two experiments. During experiment 1, the virions were tested either in the neutral extracellular environment or the acidic endosomal environment. During experiment 2, the virions were tested in the neutral extracellular environment and subsequently in the acidic endosomal environment.

Experiment 1 involved testing the virions in an environment representing the extracellular with a neutral pH. The neutral extracellular environment was represented by the buffer phosphate-buffered saline (PBS, pH 7.4, composition: 137 mM sodium chloride (NaCl), 2.7 mM potassium chloride (KCl), 10 mM sodium hydrogen phosphate (Na_2HPO_4), 1.8 mM potassium dihydrogenphosphate (KH_2PO_4)) because it is commonly used in biological research and has a useful pH range of 5.7 to 8.0 (Sigma-Aldrich 2020). PBS was only used to represent the first environment because the useful pH range does not coincide with the optimal pH fusion range of the virions.

Experiment 1 also involved testing the virions in a second environment representing the acidic endosomal with a pH that may initiate fusion. Chikungunya virus has an optimal pH fusion range of 4.5 to 5.6 (Van Duijl-Richter *et al.* 2015a) with a threshold of 6.2 (Kielian *et al.* 2010). A sub-optimal, rather than an optimal fusion pH was chosen for the second buffer because it was sufficiently acidic to allow mechanical or morphological changes to occur before the virions destabilize. The acidic endosomal environment was represented by buffer 2-(N-Morpholino)ethanesulfonic acid (MES, 50 mM, pH 6.0) because it can be used for biological research and it has a useful pH range of 5.5 to 6.7, which coincides with the optimal pH fusion range of the chikungunya virions (Sigma-Aldrich 2020). 120 mM of NaCl was added to MES to simulate similar salt conditions as in blood. The MES solution was titrated with sodium hydroxide (NaOH) until a pH of 6.0 was reached.

Experiment 2 was conducted to determine whether any changes in virion height and spring stiffness found were attributed to the change in pH of the endosomal environment. Experiment 2 involved performing nanoindentation tests on the sample initially in PBS. The PBS was subsequently removed and replaced with MES. The sample was further tested in MES. A different section of the sample was tested to ensure all the virions tested were indented once.

2.2.4. AFM Indentation Tests

The AFM work was performed on a JPK Nanowizard 3 Ultra Speed (as shown in Figure 2-4) with JPK Data Processing 6.1.79 software (Bruker Nano GmbH, Berlin, Germany). For the imaging of the sample, the AFM was in peak force tapping mode whereas, for indentation of the virions, the AFM was in force spectroscopy mode. The experiments were performed in a fluid environment using cantilever qp-BioAC-20 CB2 with a spring constant of 0.1 N/m. The cantilever was cleaned or replaced and calibrated for each sample.

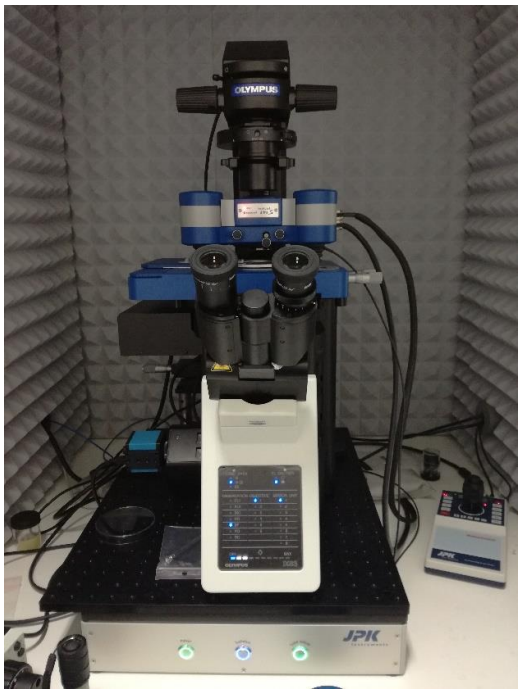

Figure 2-4: *JPK Nanowizard 3 Ultra Speed in the acoustic hood. The acoustic hood was the housing unit and responsible for temperature control throughout the experiments.*

The sample was imaged to locate virions. Each virion identified for the indentation experiment was isolated and imaged. An indentation experiment was performed on the coverslips and then in the centre of the virion. An image was taken after the indentation experiment to view changes caused by the experiment. An image of a virion before and after the experiment is shown in Figure 2-5.

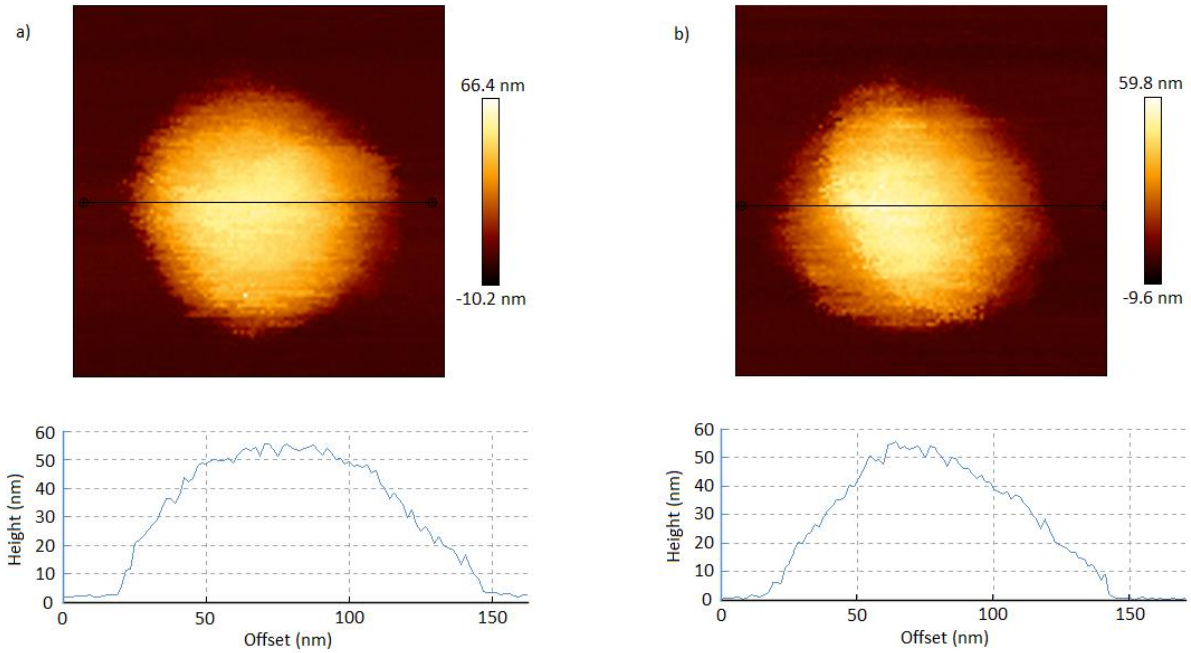

Figure 2-5: *Isolated chikungunya virion on a glass coverslip. The picture represents Test 17 of the virion a) before and b) after the nanoindentation experiment in PBS with with graphs representing the respective cross-sectional height. The black horizontal line on the image indicates where the cross-section was obtained. A nanoindentation test was first performed on the glass coverslip (dark) then the centre of the virion (bright). The scale bar is indicated on the right of the picture.*

The force-displacement (FD) curves for the nanoindentation experiment of the glass coverslips and virion is shown in Figure 2-6.

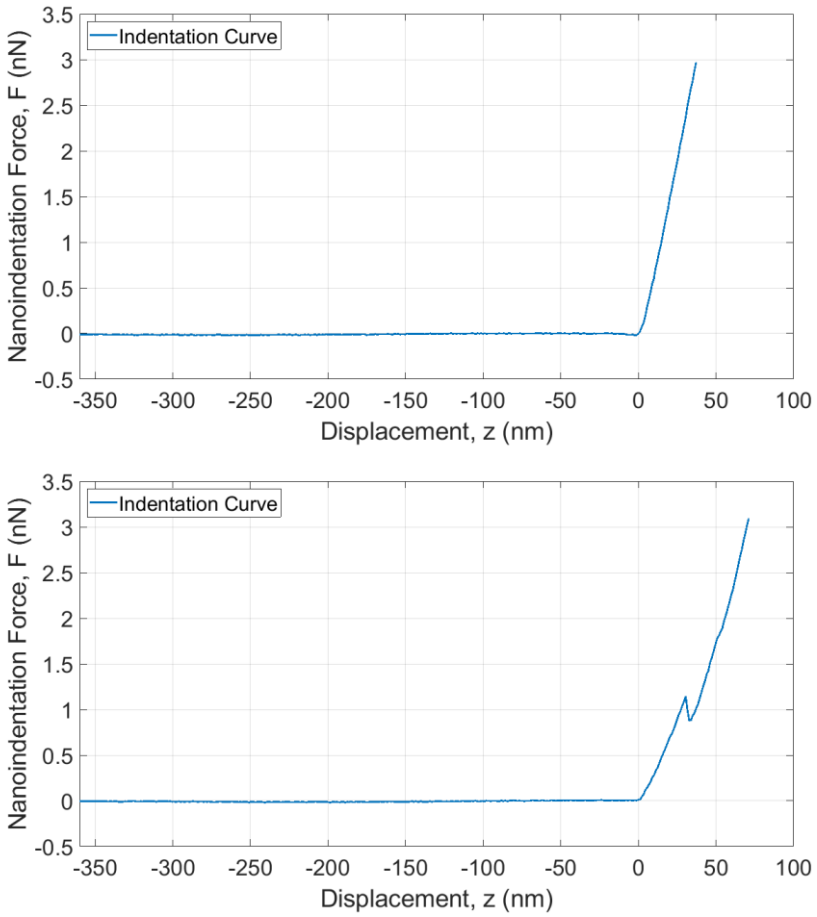

Figure 2-6: *Force-displacement curve for a) the glass coverslip and b) the virion. The graphs represent Test 1 of the virions tested in MES.*

2.2.5. Data Analysis

The FD data were exported from the JPK software, and a linear fit was performed on each virion curve.

The linear fit of the graph was between 0.1 and 0.4 nN, as shown in Figure 2-7.

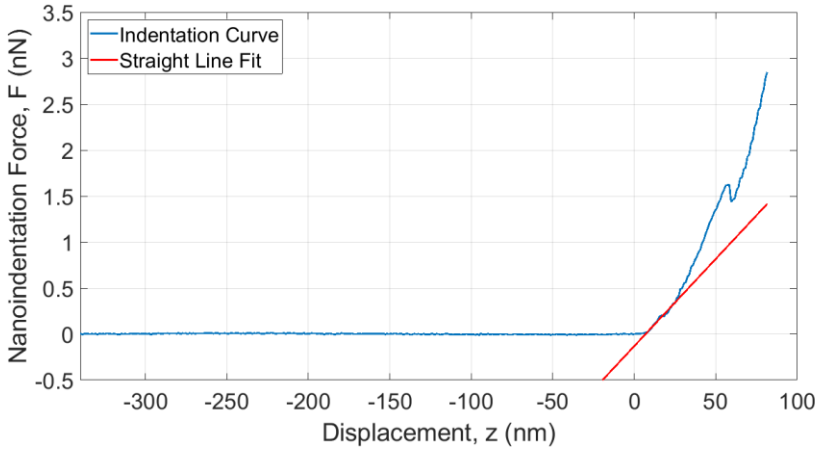

Figure 2-7: *Force-displacement curve with a linear fit for Test 21 of the virions tested in PBS. The linear fit of the graph was between 0.1 and 0.4 nN. The spring constant of the total system, determined by the slope of the linear fit, was* $k_t = 0.01896$ *N/m.*

The spring constant of the virus (k_v) was determined from the initial linear slope of the curve (as shown in Figure 2-7), which represents the spring constant of the whole system (k_t). Therefore, using Hooke's Law for two springs in series, the spring constant of the virion (k_v) was determined as follows:

$$k_v = \frac{k_t . k_c}{k_c - k_t}$$

During imaging of the virion, the force applied by the cantilever causes the virion to deform, therefore reducing the cross-sectional height of the virion obtained from the image. As a result, the height obtained from the image does not represent the actual height of the virion. Hence, the cross-sectional height was not reported, however it was used to determine the actual height of the virion (h_v) as follows:

$$h_v = h_{xs} + \frac{F_i}{k_v}$$

where h_{xs} was the cross-sectional height of the virion from the image, as shown in Figure 2-5, and F_i was the force applied by the cantilever onto the virion during imaging.

During the nanoindentation tests, viruses can display a two phase force-indentation response before the failure point, as shown in Figure 2-8 (Li *et al.* 2014, Schaap *et al.* 2012). It was proposed that the first phase indicates the mobilisation of the ectodomain and represents the virion deforming elastically (Schaap *et al.* 2012). It was also proposed that the second phase represents the virion once the ectodomain is removed and the virion deforms plastically (Schaap *et al.* 2012).

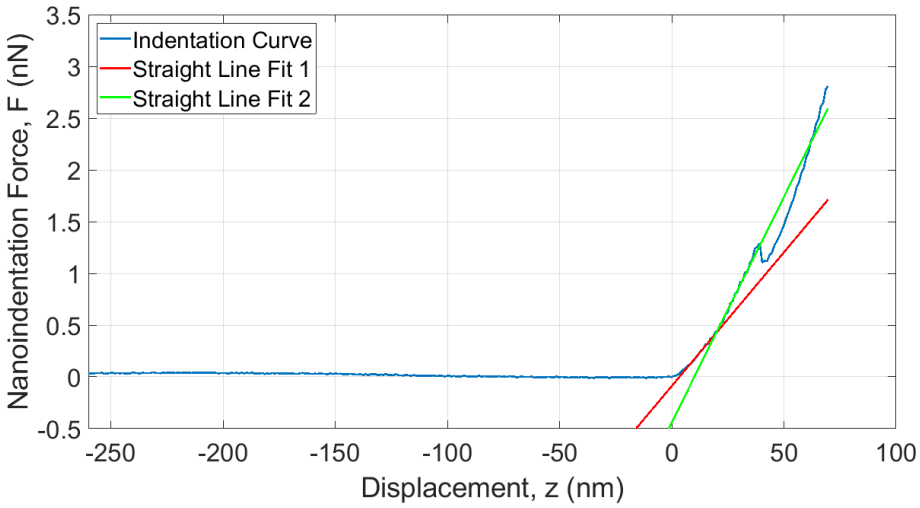

Figure 2-8: *Force-displacement curve with two linear fit lines. The graph represents Test 18 of the nanoindentation experiments of the virions in PBS. The first linear fit (red) of the graph was between 0.1 and 0.4 nN. The second linear fit (green) was between 0.4 nN and the breaking point. The virion spring constant of Test 18 using the first linear fit (red) was k_v= 0.035 N/m while the spring constant of the virion using the second linear fit (green) was k_v= 0.077 N/m.*

2.2.6. Statistical Analysis

Data are provided as mean ± standard deviation (SD) unless otherwise indicated. For the statistical analysis, the Shapiro-Wilk test was performed to determine whether the data has a normal Gaussian distribution. A P-value of greater than .05 indicates a normal Gaussian distribution. A factorial ANOVA (analysis of variance) was conducted to determine how the height of the virion is affected by the following factors:

1. Change in pH of the endosomal environment (PBS vs MES for experiment 1).
2. Before and after the nanoindentation test was performed.
3. Whether the virions were part of experimental group 1 or experimental group 2.

A factorial ANOVA was also conducted to determine how the spring constant is affected by these factors:

1. Change in pH of the endosomal environment (PBS vs MES for experiment 1).
2. Suppose there was a change in the slope of the FD curve for the virions tested in PBS. The spring constant of the virions was calculated for an indentation force between 0.1 and 0.4 nN however, the slope of the FD curve may change from after initial contact between the cantilever tip and virion to when the virion reaches the breaking point.
3. Whether the virions were part of experimental group 1 or experimental group 2.

A P-value of less than .05 for the simple main effects and interaction effects was assumed to indicate a significant statistical difference in mean of the variables. Data are provided as F (df, error) = F–value, p-value, η_p^2 = partial eta squared (effect size for analysis of variance). The degree of freedom (df) was reported for the simple main effects and in most cases will be df = 1. Partial eta squared was interpreted as .01 for small effect size, .09 for medium effect size and .25 for large effect size. The Pearson Correlation test assessed the correlation between the virion height and spring constant. A P-value of less than .05 indicates a significant correlation.

2.3. Results

During the nanoindentation tests for experiment 1, 25 virions were tested in PBS, and 2 outliers were found. 38 virions were tested in MES, and 1 outlier was found. The samples tested in PBS (n = 23) and MES (n = 37) were obtained on 5 days from samples from 3 aliquots. In total, 60 FD curves were analysed. During experiment 2, 6 virions were tested in PBS, and 9 virions were tested in MES from 1 aliquot tested on the same day. In total, 15 FD curves were analysed.

2.3.1. Height

The results for experiment 1 of the actual height of the virions tested in PBS and MES is presented in Figure 2-9. The actual height (h_v) of the virions tested in PBS was 57.8 ± 3.0 nm and in MES was 46.0 ± 5.1 nm.

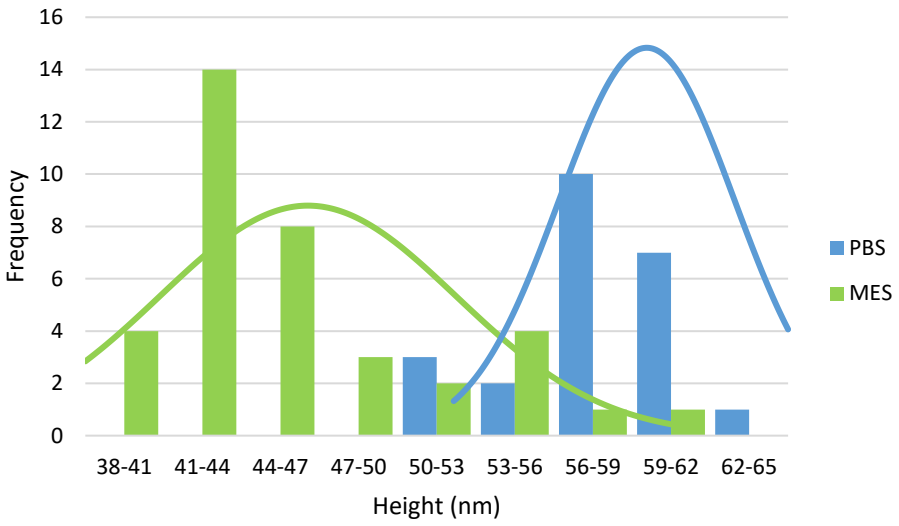

Figure 2-9: *Histogram and Gaussian's curve of the height of the virions tested in PBS and MES. The histogram represents the actual heights of the virions tested in PBS and MES. The actual height of the virions in PBS was 57.8 ± 3.0 nm and in MES was 46.0 ± 5.1 nm.*

The actual height of the virions tested in PBS and MES after the nanoindentation test was performed was 48.7 ± 10.3 nm and 41.6 ± 4.0 nm, respectively. Figure 2-10 illustrates the comparison of the actual heights of the virions tested in PBS and MES before and after the nanoindentation experiments.

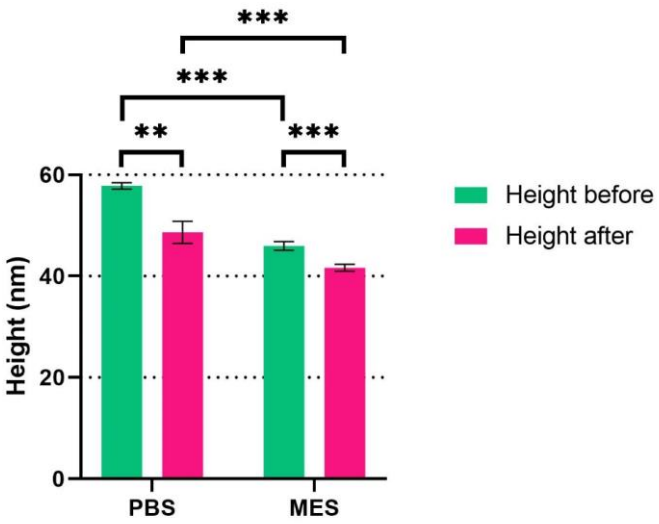

Figure 2-10: *A bar graph of the actual height of the virions tested in PBS and MES before and after the nanoindentation experiments. The actual height of the virions in PBS was 48.7 ± 10.3 nm and in MES was 41.6 ± 4.0 nm. The error bars indicate SEM. *p = < .05, **p = < .005, ***p = < .0005.*

A factorial ANOVA was performed on the actual height data that was transformed using the align and rank process. The ANOVA analysed whether the height of the virions was dependant on the buffer, experimental group or force exerted by the cantilever during the nanoindentation test. The simple main effects analysis indicated there was a statistically significant difference between the virions tested in PBS and MES ($F(1,139) = 51.5$, $p < .001$, $\eta_p^2 = .27$). There was no significance between the interactions. A simple main effects analysis also showed that there was a statistically significant difference between the virions tested in PBS and MES before ($p < .001$), and after ($p < .001$) the nanoindentation experiments were performed. The height of the virions before (57.8 ± 3.0 nm) the nanoindentation experiment were significantly higher than the virion heights after (48.7 ± 10.3 nm) the experiment was performed ($F(1, 139) = 26.9$, $p < .001$, $\eta_p^2 = .16$).

For experiment 2, the actual height of the virions tested in PBS was 55.8 ± 3.7 nm and in MES was 47.2 ± 4.3 nm for the second experiment. The results of the actual height of the virions tested in the second experiment compared to the first experiment are presented in Figure 2-11.

The simple main effects analysis showed that there was no statistically significant difference between experiment 1 and 2 ($F(1, 139) = 1.014$, $p = .32$, $\eta_p^2 = .007$). When tested in PBS, the actual height of the virions in experiment 1 and 2 before ($p = .65$) and after ($p = .96$) the nanoindentation experiment was performed were similar. When tested in MES, the actual height of the virions in experiment 1 and 2 before ($p = .32$) and after ($p = .53$) the nanoindentation experiment was performed were also similar. For the second experiment, the virions tested in PBS showed no difference in the actual heights before and after the nanoindentation experiment was performed ($p = .089$).

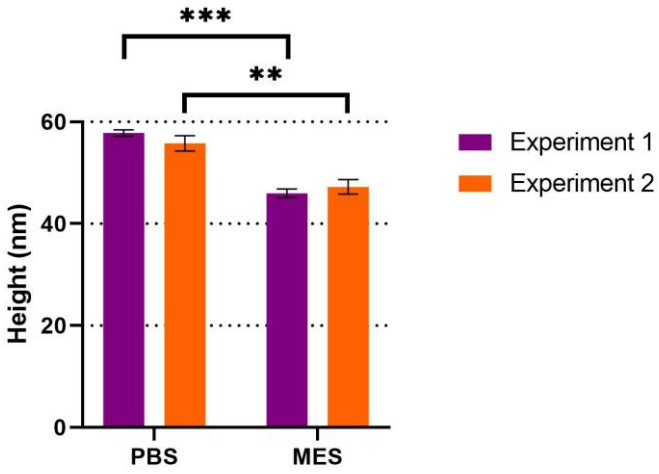

Figure 2-11: *A bar graph representing the actual height of virions tested in PBS and MES for experiment 1 and 2. The virions were tested in PBS, the buffer was then removed, and MES was added for further testing. The height of the virions in PBS was 55.8 ± 3.7 nm and in MES was 47.2 ± 4.3 nm. The error bars indicate SEM. *p = < .05, **p = < .005, ***p = < .0005.*

2.3.2. Spring Constant

The results of the spring constant of the virions tested in PBS and MES are presented in Figure 2-12. The spring constant of the virions tested in PBS was 0.035 ± 0.012 N/m and in MES was 0.047 ± 0.017 N/m.

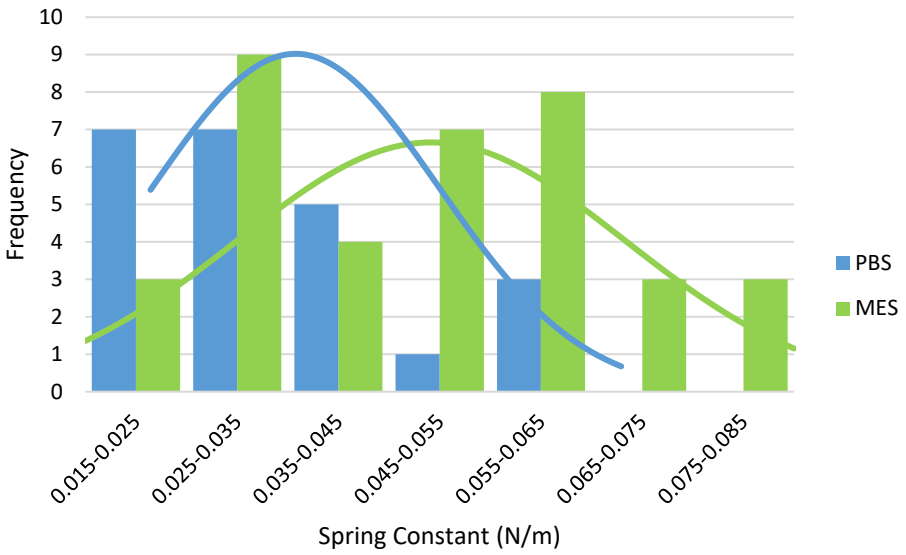

Figure 2-12: *Histogram and Gaussian's curve representing the spring constant of the virions tested in PBS and MES. The histogram represents the spring constant of the virions tested in PBS and MES. The spring constant of the virions in PBS 0.035 ± 0.012 N/m and MES was 0.047 ± 0.017 N/m.*

During the nanoindentation tests, 20 of the 23 virions tested in PBS indicated two slopes before the failure point, as shown in Figure 2-8. The spring constant of the virions calculated using the slope of the second section from the FD curve was 0.061 ± 0.021 N/m.

For the second experiment, the spring constant of the virions tested in PBS was 0.033 ± 0.010 N/m and in MES was 0.045 ± 0.015 N/m. Most of the virions tested in PBS during the second experiment also indicated two slopes before the failure point. Of the 6 virions tested in PBS, 5 were used to calculate the spring constant of 0.066 ± 0.015 N/m. Figure 2-13 illustrates the spring constants of the virions tested in PBS and MES for experiments 1 and 2.

A factorial ANOVA was performed on the inversely transformed spring constant data. The analysis showed there was a statistically significant difference between the virions tested in PBS and MES ($F(1, 94) = 5.235$, $p = .024$, $\eta_p^2 = .053$). A simple main effects analysis indicated that for the first experiment, the spring constant of the virions tested in PBS is significantly lower than the virions tested in MES ($p = .037$). For experiment 2, the spring constant of the virions tested in PBS and MES were similar ($p = .14$). There is a statistically significant difference between slope 1 and 2 for the virions

tested in PBS during experiment 1 ($p < .001$) and experiment 2 ($p = .006$). The spring constants of the virions in experiment 1 were similar to the spring constants of the virions tested in experiment 2 for PBS slope 1 ($p = .576$), PBS slope 2 ($p = .621$) and MES ($p = .999$).

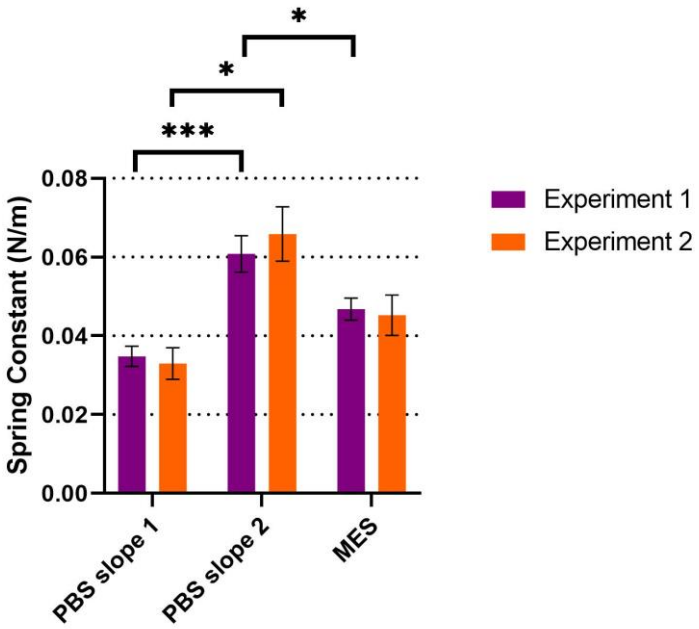

Figure 2-13: *A bar graph representing spring constant of the virions tested in PBS (slope 1 and 2) and MES. For experiment 1, the spring constant of the virions in PBS slope 1 was 0.035 ± 0.012 N/m, PBS slope 2 was 0.061 ± 0.021 N/m and in MES was 0.047 ± 0.017 N/m. For experiment 2, the spring constant for PBS slope1 was 0.033 ± 0.010 N/m, PBS slope 2 was 0.066 ± 0.015 N/m and in MES was 0.045 ± 0.015 N/m. The error bars indicate SEM. *p = < .05, **p = < .005, ***p = < .0005.*

2.3.3. Correlation between Height and Spring Constant

The Pearson correlation test indicated that there was no correlation between the virion height and spring stiffness (slope 1) for the virions tested in PBS ($p = .46$) and in MES ($p = .13$), which is illustrated by the straight line in Figure 2-14 and Figure 2-15, respectively.

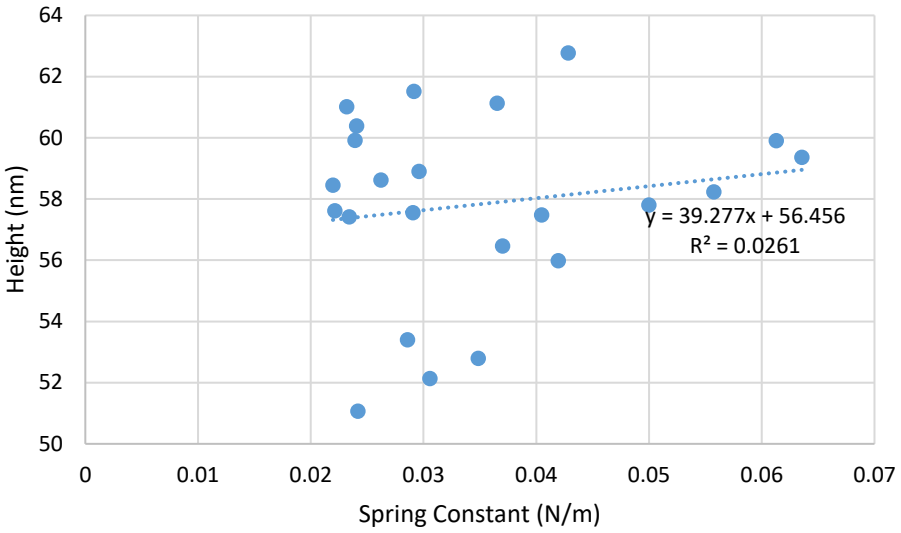

Figure 2-14: *Correlation of height and spring constant (slope 1) for the virions tested in PBS. The Pearson Correlation test indicated there was no correlation between the heights and spring constant of the virions tested in PBS. The p-value was .46, and R^2 was .026.*

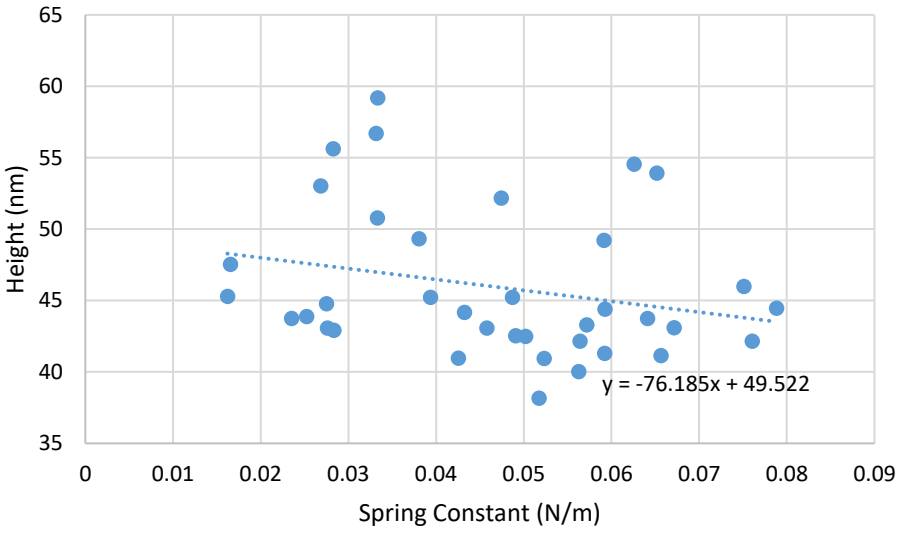

Figure 2-15: *Correlation of height and spring constant (slope 1) for the virions tested in MES. The Pearson Correlation test indicated there was no correlation between the heights and spring constant of the virions tested in MES. The p-value was .13, and R^2 was .063.*

2.4. Discussion

This study aimed to characterise the mechanical properties of chikungunya virus-like particles in different endosomal environments. The endosomal environments were represented by the buffers PBS and MES. PBS with pH 7.4 represented the neutral extracellular environment which did not promote fusion. MES with pH 6.0 represented the acidic endosomal environment which promotes fusion.

2.4.1. Height

During the experiment, 23 FD curves were analysed for the virions tested in PBS. The height of chikungunya virions according to literature (60 – 70 nm) was greater than the actual height of the tested virions (57.8 ± 3.0 nm). This could be a result of the envelope glycoproteins being squashed or pushed aside under the pressure of the cantilever during the nanoindentation tests. Schaap *et al.* (2012) illustrated the response of Influenza virions being indented. As shown in Figure 2-16, the force applied during indentation could cause the envelope proteins to be pushed, which may result in a disparity in virion heights.

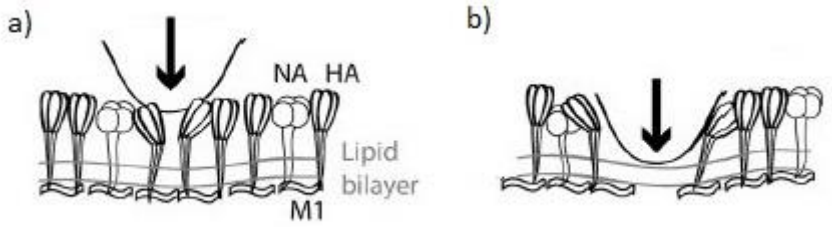

Figure 2-16: *Response of envelope glycoproteins due to an external force. a) The indenter makes contact with the virion. b) The indenter pushes/squashes the envelope proteins. With permission from Schaap et al. (2012).*

For the virions tested in MES, 37 FD curves were analysed. After comparing a typical structural breakdown of the chikungunya virion (see Figure 2-1) to the height (46.0 ± 5.1 nm) of the tested virions, it was found that the mean height of the tested virion corresponds with the diameter of the capsid containing the viral genome (40.2 nm). This could suggest that the spring constant of the virions tested in MES represents the spring constant of the capsid, including the viral genome. This could also indicate that the capsid and viral genome is stiffer than the whole virion.

The E1 and E2 glycoproteins and the membrane consists of alpha-helices (Albers 2012). The length of a helical segment can span the width of the viral membrane, and its side chains determine the surface properties of the membrane (Albers 2012). Each helical segment that traverses the membrane consists of hydrophobic residues (Albers 2012). Conformational changes in the E1/E2 glycoproteins were induced by the acidic pH, which results in the dissociation of the glycoproteins (Kuo *et al.* 2012). The extremely hydrophobic membrane region could cause it to associate strongly with the glycoproteins and the membrane may have been removed when the glycoproteins dissociate. This could suggest that the capsid is delivered into the cytoplasm after fusion of the virion and endosomal membranes. This may also suggest that the virions tested in MES consisted of the viral genome enclosed by the capsid.

A factorial ANOVA showed that the results from experiment 2 correspond with the results of the virions tested in PBS and MES in experiment 1. This suggests that the difference in the height of the virions tested in PBS (57.8 ± 3.0 nm) and MES (46.0 ± 5.1 nm) were the result of the change in pH of the buffer. However, only a few virions were tested during the second experiment, and it is suggested that more virions are tested in future experiments to support this finding. There was also a significant difference between the virion height before (57.8 ± 3.0 nm and 46.0 ± 5.1 nm) and after (48.7 ± 10.3 nm and 41.6 ± 4.0 nm) the nanoindentation tests were conducted in both PBS and MES. This indicates that the virions may have been flattened or plastically deformed under the pressure of the indentation force.

2.4.2. Spring Constant

Limited information on chikungunya virus prevents comparison of the experimental spring constant to literature; however, the spring constant was comparable to other viruses, as shown in Table 2-1. The spring constant for the viral capsid of CCMV, HBV, Bacteriophage HK97 and φ29 (Prolate) was determined as well as the spring constant for the enveloped viruses, HIV and influenza virus.

Table 2-1: Spring constant of chikungunya virus compared to other viruses.

Virus name	Spring constant (N/m)	Reference
Chikungunya virus (CHIKV)	0.035	
Human immunodeficiency virus (HIV)	0.22	(Kol *et al.* 2007)
Cowpea chlorotic mottle virus (CCMV)	0.13-0.17	(Snijder *et al.* 2012)
Influenza virus	0.02	(Schaap *et al.* 2012)
Bacteriophage HK97	0.10-0.16	(Snijder *et al.* 2012)
Bacteriophage φ29 (Prolate)	0.20-0.24	(Snijder *et al.* 2012)
Hepatitis B virus (HBV)	0.09	(Arkhipov *et al.* 2009)

A statistical analysis indicated that there was a significant difference in spring constant between the virions tested in PBS (0.035 ± 0.012 N/m) and MES (0.047 ± 0.017 N/m). The increase in stiffness of the virions, which is associated with a decrease in virion height, may indicate that the smaller configuration is more structurally stable. Similar to the virion height, the analysis indicated there was no significant difference in spring constant between experiment 1 and 2, suggesting the changes in spring constant were the result of the change in pH of the buffer. For most of the virions tested in PBS, two slopes were obtained on the FD curve (see **Error! Reference source not found.**). The spring constant of the virions calculated using the second slope (0.061 ± 0.021 N/m) was greater than the spring constant for the first slope (0.035 ± 0.012 N/m), and the virions tested in MES (0.047 ± 0.017 N/m), however closer to the virions tested in MES.

The spring constant for the first slope in PBS could represent the stiffness of the entire virions while the second slope could represent the stiffness of the membrane and capsid after the glycoproteins have been pushed aside (see Figure 2-16). The spring constant for the virions tested in MES could represent the stiffness of the capsid, after dissociation of the envelope glycoproteins along with the membrane. The membrane may have a strong affinity to associate to the glycoproteins when they dissociate due to its hydrophobic properties and the nature in which the glycoproteins were embedded into the membrane (Albers 2012, Kuo *et al.* 2012). The spring constant for the virions tested in MES could also represent the stiffness of the capsid with partial dissociation of the envelope glycoproteins. The spring constant for the virions tested in MES may be stiffer than the first slope in PBS due to only the capsid being indented, however softer than the spring constant for the second slope in PBS because the glycoproteins were absent. Other enveloped viruses, such as HIV, have also shown a decrease in stiffness with an absence of glycoproteins (Kol *et al.* 2007).

2.4.3. Correlation between Height and Spring Constant

There was no correlation between the height and spring constant of the virions tested in PBS and MES. This could be because of the limited sample size and repeating the experiment with a larger size might indicate a correlation.

3. Development of 3D Geometric Model and Computational Simulations of Chikungunya Virions

3.1. Introduction

Studying 3D geometric models of virions provide insight into the structures of the virion at near-atomic resolution. Geometric models can be reconstructed using images generated using cryogenic electron microscopy (cryo-EM). Cryo-EM involves using electron microscope (EM) techniques to samples frozen to cryogenic temperatures. This allows for the visualisation of biological structures at near-atomic resolution. The geometric models can be used in finite element (FE) modelling to generate computational simulations of static or dynamic phenomenon.

3.2. Materials and Methods

This section covers the reconstruction of 3D geometric models and the methodology used to develop the model for the computation simulations.

3.2.1. Geometric Modelling

A 3D geometric model of a chikungunya VLP was reconstructed from image data obtained from the Protein Data Bank Japan[3] using UCSF Chimera (Pettersen *et al.* 2004) and Simpleware ScanIP (Synopsys Inc). Jin *et al.* (2015) generated cryo-EM data of a 3D topographical map of a chikungunya VLP at 15.3 Å resolution (EMDB-6466). VLPs have a similar structure as the WT virus however lack the RNA. One slice of the data is shown in Figure 3-1.

Figure 3-1: *Cryo-EM image slice of chikungunya VLP. The EM data, generated by Jin et al. (2015), was found in Protein Data Bank Japan (EMDB-6466). From Protein Data Bank Japan (2015).*

[3] For more information on Protein Data Bank Japan, see https://www.rcsb.org/

Using UCSF Chimera, the cryo-EM data generated by Jin *et al.* (2015) was used to reconstruct only the envelope of the VLP. The model was used for computational simulations which require the model to be a continuous solid to allow for adequate meshing. As a result, the inside of the model was filled as part of the image processing. Image processing was completed using Simpleware ScanIP, and the process included using functions such as "fill", "close", and "smooth" to ensure the reconstructed geometry does not contain discontinuities. Figure 3-2 illustrates the geometry before and after the "fill" function was applied.

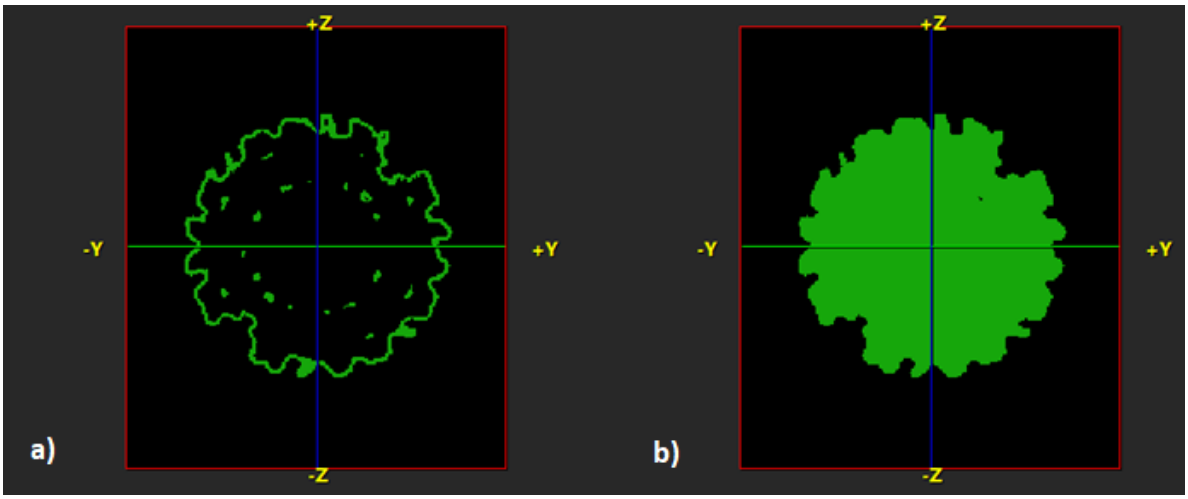

Figure 3-2: *Cross-section view of the geometric model. The image displays the model a) before and b) after the "fill" function was applied.*

Other cross-sectional views indicate that there were still discontinuities inside the model, as shown by the red circles in Figure 3-3. Functions such as "close" and "smooth" were used to remove remaining discontinuities and render a smooth VLP surface.

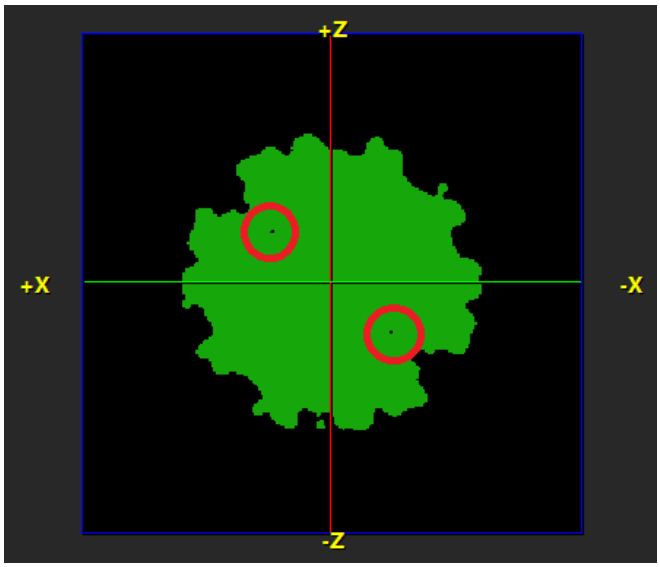

Figure 3-3: *Cross-section of the filled model with discontinuities. The red circles indicate discontinuities found in the model after the "fill" function was performed.*

3.2.2. Finite Element Modelling

Using finite element (FE) models, computational simulations of an AFM experiment were undertaken to study the indentation behaviour of the chikungunya VLP. Simulations were conducted using Abaqus/CAE 6.14.3 (Dassault Systèmes, Vélizy-Villacoublay, France).

3.2.2.1. Model Geometry

The finite element model to simulate *in vitro* experiments comprised of three components: the chikungunya VLP, the substrate and the cantilever tip/indenter. The reconstructed chikungunya VLP geometry with an outer diameter of 63 nm was imported into Abaqus/CAE from Simpleware ScanIP. The substrate was modelled as a 100 nm × 100 nm × 20 nm rectangular body. The indenter was modelled as a sphere with a diameter of 10 nm, which corresponds to the radius of curvature of the AFM cantilever used during the nanoindentation experiments described in Chapter 2. The VLP rested in the centre of the substrate, and the indenter was positioned above the centre of the VLP. No sliding was permitted at the interfaces of the surfaces of the components. The complete model is shown in Figure 3-4.

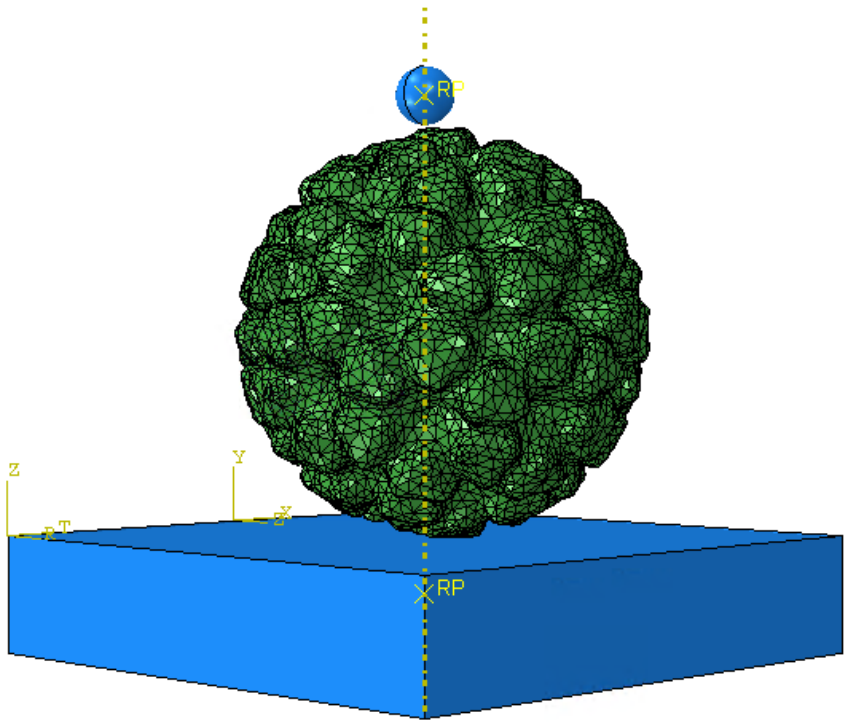

Figure 3-4: *FE model for simulation of nanoindentation experiment comprising reconstructed VLP (green), indenter sphere and rectangular substrate (both blue).*

3.2.2.2. Mesh Generation

The VLP, indenter and substrate were meshed separately. The VLP was meshed in Simpleware ScanIP and imported into Abaqus/CAE. The mesh consisted of four-node tetrahedral elements. The indenter and substrate were meshed in Abaqus/CAE. The mesh of the indenter and substrate consisted of ten-node tetrahedral and linear brick elements, respectively. Table 3-1 summarizes the type and number of elements for each component in the model.

Table 3-1: Types and number of elements for the components in the model.

Component	Type of Element	Number of Elements
VLP	C3D4	63,439
Indenter	C3D10	139
Substrate	C3D8R	9

The meshed indenter, VLP and substrate are shown in **Error! Reference source not found.**.

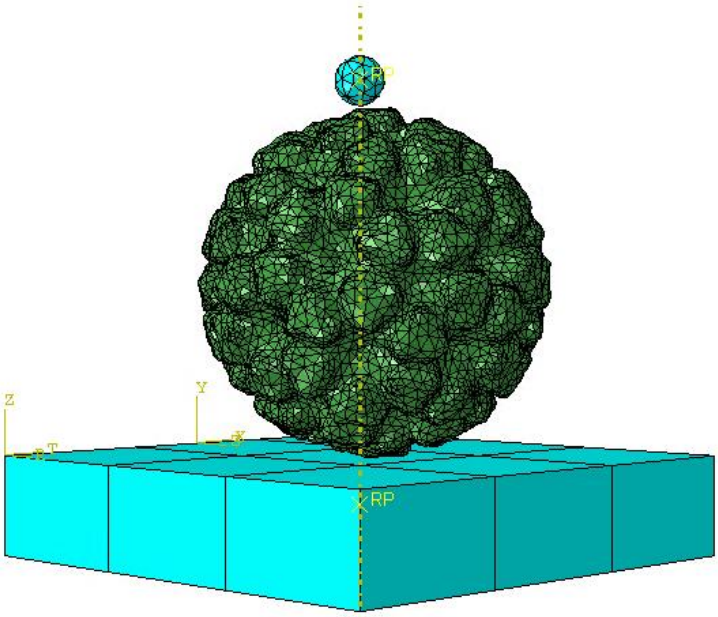

Figure 3-5: *The computational model, including mesh. The spherical indenter has 139 elements, and the rectangular substrate has 9 elements. The reconstructed VLP had a diameter of 63 nm. The substrate was a 100 nm × 100 nm × 20 nm rectangular body. The indenter was a sphere with a diameter of 10 nm.*

3.2.2.3. Material Properties

The VLP was assumed to be isotropic linear elastic. The two material parameters, elastic modulus (E_V) and Poisson's ratio (ν_v) were calibrated for the VLP. Only one parameter was calibrated at a time; therefore, the value for Poisson's ratio was chosen, and the elastic modulus was calibrated to experimental data. Viral capsids are slightly compressible; therefore, the practical choice for Poisson's ratio was 0.3 to 0.4 (Ahadi *et al.* 2009).

The substrate and indenter were modelled as rigid, non-deformable bodies. Typically, rigid bodies do not have material properties, however due to the Abaqus/CAE software requirements, a material model was prescribed. Nevertheless, the material properties assigned to the rigid bodies have no effect on the simulation. The substrate and indenter were assumed to be isotropic linear elastic and were assigned the material properties of glass and quartz (Nanosensors™ 2013), respectively. This corresponds with the type of material which constituted the substrate and cantilever tip from the nanoindentation experiments. Table 3-2 summarizes the material properties of the components in the model.

Table 3-2: Material properties of the components in the model.

Component	Constitutive Law	Material Parameters	Reference
VLP	Linear Elastic	ν_v = 0.3, 0.35, 0.4	(Ahadi *et al.* 2009)
Indenter	Linear Elastic	E_i = 72 GPa; ν_i = 0.17	(San Jose Delta 2017)
Substrate	Linear Elastic	E_s = 70 GPa; ν_s = 0.22	(Engineering Toolbox 2003, 2008)

3.2.2.4. Boundary Conditions and Loading

The *in silico* analysis was modelled to simulate *in vitro* experiments. Boundary conditions were applied to the model to simulate the movement from the *in vitro* experiments. The model was governed by a cylindrical coordinate system. The cylindrical coordinate system was used to describe the rotational and tangential movement of the VLP and the axial movement of the indenter. The T_C-, Z_C- and R_C-axis of the cylindrical coordinate system corresponds with the X-, Y-, and Z-axis of the rectangular coordinate system, respectively, and is illustrated in Figure 3-6.

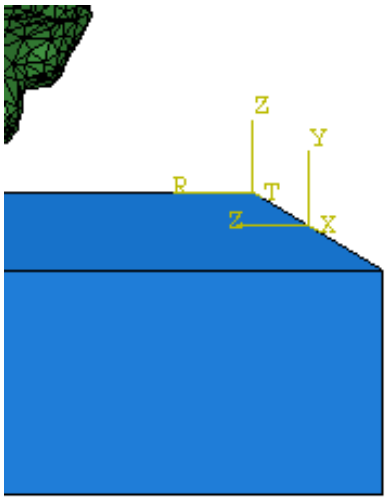

Figure 3-6: *The coordinate system of the model. The model employs the cylindrical coordinate system represented by the T_C-, Z_C- and R_C-axis which corresponds with the X-, Y-, and Z-axis from the default rectangular coordinate system.*

Displacement and rotation boundary conditions were applied to each component of the model. For the substrate, no movement was permitted. For the VLP and the indenter, translation was permitted in Z_C-direction whereas translations in R_C- and T_C-direction and rotation around all three axes was not permitted. For the indenter and the substrate, the boundary conditions were applied to the reference point in the centre of indenter and substrate, respectively. For the VLP, the boundary conditions were applied to every node in the geometry. Figure 3-7 illustrates the boundary conditions in the model.

The loading was represented as the displacement of the indenter in negative Z_C-direction. The average value of the displacement corresponding with an indentation force of 0.4 nN of the *in vitro* experiments conducted in PBS (see Chapter 2) was used as the maximum loading *in silico*.

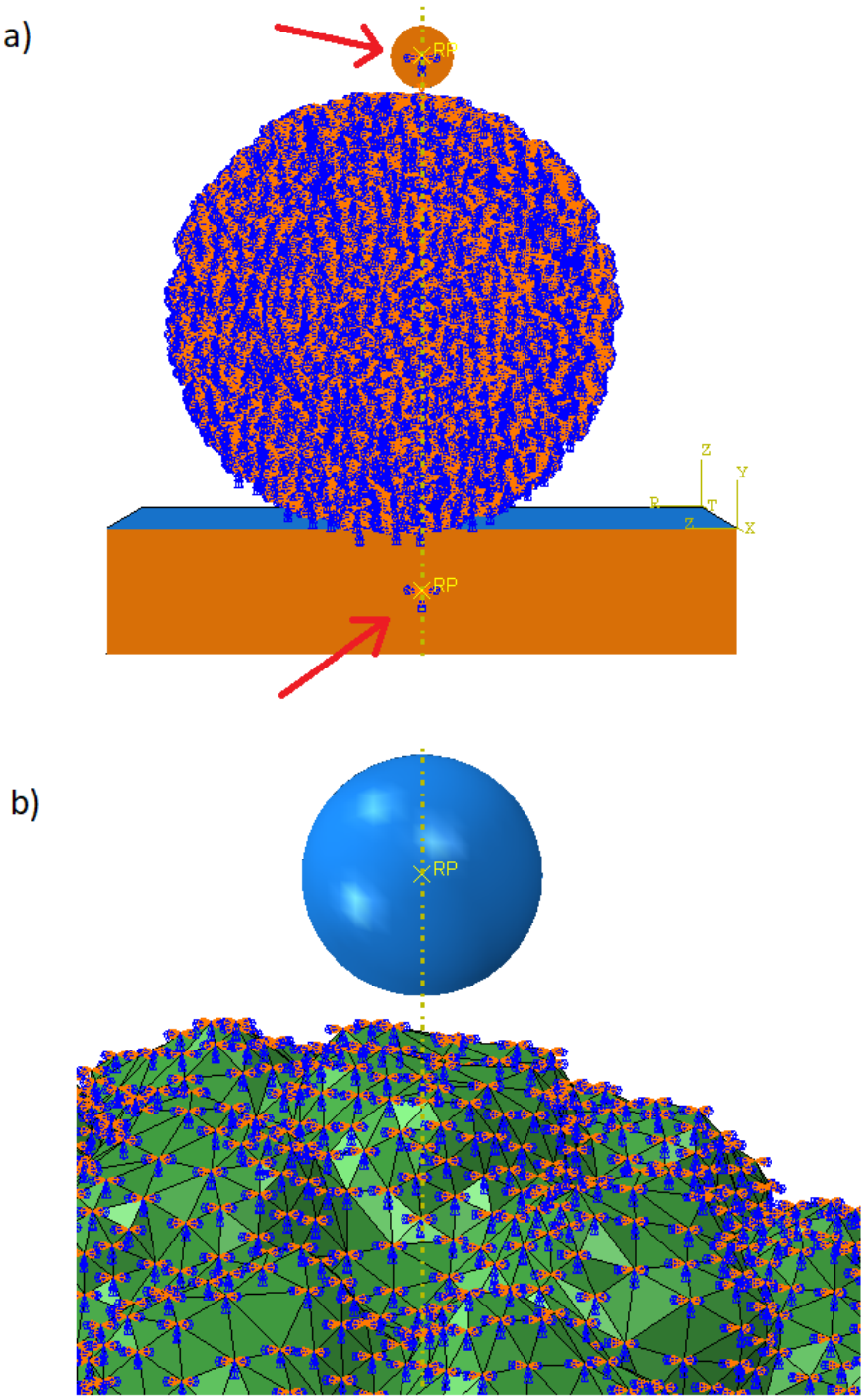

Figure 3-7: *Illustration of boundary conditions. a) Cross-sectional view of the indenter, VLP and substrate, showing the boundary conditions applied to the reference point of indenter and substrate, respectively, indicated by the red arrows, and to internal nodes in the cross-sectional surface of the VLP. b) Boundary conditions on surface nodes of VLP.*

3.2.2.5. Data Acquisition and Analysis

The loading applied by the indenter *in silico* was interpolated from the *in vitro* FD curves. The average value of the displacement corresponding with an indentation force of 0.1 and 0.4 nN *in vitro* were also determined to compare the extent to which the *in silico* results deviate/converge from/to the *in vitro* results. Figure 3-8 shows an FD curve obtained from the experimental tests, and the data points nearest to an indentation force of 0.1 nN and 0.4 nN found to calculate the displacement.

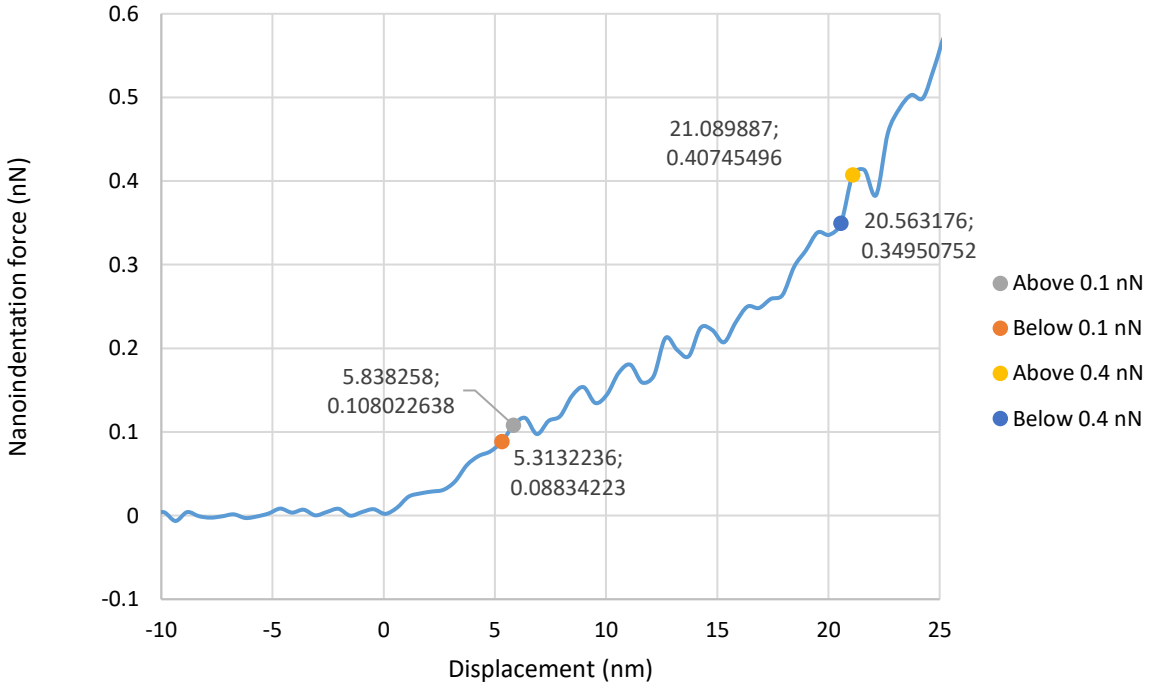

Figure 3-8: *Force-displacement curve for the first VLP tested in PBS. Displayed were the data points used to interpolate the displacements at an indentation force of 0.1 nN and 0.4 nN. The coordinates are shown as (X; Y).*

The FE models were calibrated to provide FD curves, and a spring constant corresponding with the *in vitro* studies of the VLPs tested in PBS (k_v = 0.035 N/m). The results were extracted from the reference points of the indenter and substrate, namely the prescribed displacement of the indenter and the reaction force from the substrate. The data was used to generate FD curves. The spring constant of the VLP was calculated from the slope of a straight line fit of the curve between 0.1 and 0.4 nN, which corresponds with the data analysis of the experimental indentation results. An example of the FD curve is shown in Figure 3-9.

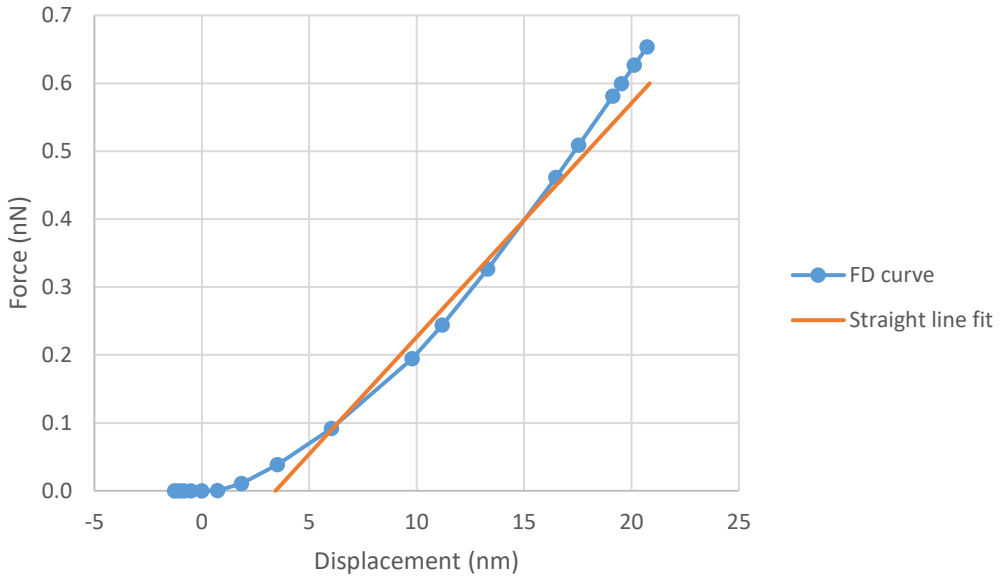

Figure 3-9: *Force-displacement curve with a straight-line fit. The curve is indicated by the dotted blue line, and the straight-line fit is indicated by the orange line. The straight line is fit between 0.1 and 0.4 nN.*

The elastic modulus of the chikungunya virus was also approximated using the thin shell model (Landau and Lifshitz 1986). The thin shell model assumed the shell of the virus is thin and elastic, and only experienced small deformations. The elastic modulus was related to the spring constant in the following equation:

$$E_t = \frac{k_v R}{\alpha t^2}$$

where E_t is the elastic modulus, k_v is the spring constant of the virus, R is the radius of the virus, α is the proportionality factor assumed to be 1, and t is the thickness of the membrane. The value of k_v was the spring constant of the virus *in vitro* (obtained from slope 1 of the viruses tested in PBS during experiment 1). The value for R and t were determined using Figure 2-1.

3.3. Results

3.3.1. Development of 3D Geometric Models

The 3D geometric model of a chikungunya VLP reconstructed using UCSF Chimera is shown in Figure 3-10.

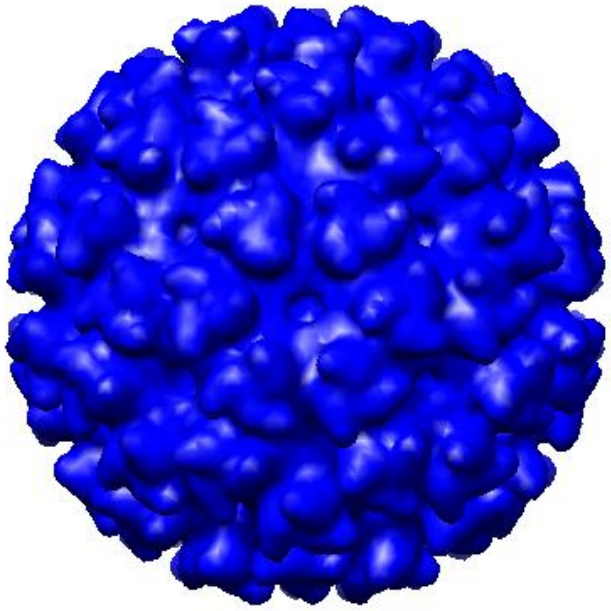

Figure 3-10: *The 3D geometric model of a chikungunya VLP reconstructed using UCSF Chimera from cryo-EM data generated by Jin et al. (2015).*

The geometric model in Figure 3-10 was exported from UCSF Chimera and processed and meshed in Simpleware ScanIP using four-node tetrahedral elements, and the model comprised 63,439 elements. Figure 3-11 shows the geometric model after meshing.

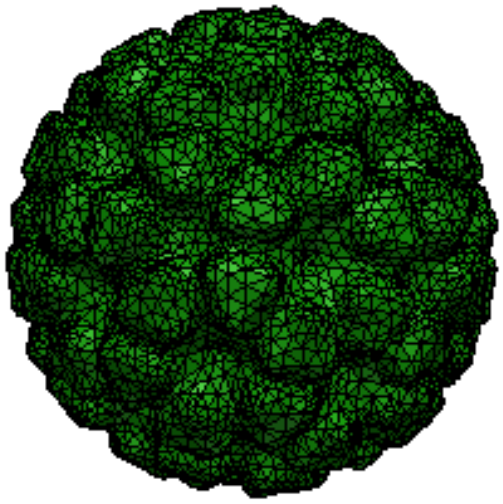

Figure 3-11: *Meshed 3D geometric model of chikungunya VLP. The model has 63,439 four-node tetrahedral shaped elements.*

3.3.2. Finite Element Modelling

The FE analysis was modelled to simulate AFM nanoindentation experiments. The mean displacement experienced by the VLPs *in vitro* at an indentation force of 0.1 nN and 0.4 nN was 7.5 nm and 20.1 nm, respectively. *In silico*, the indenter was positioned 1.3 nm above the VLP; therefore, the maximum loading applied to the indenter was 22 nm to ensure the mean indentation depth was covered. Figure 3-12 shows the cross-sectional view of the VLP at various stages of indentation during the simulation.

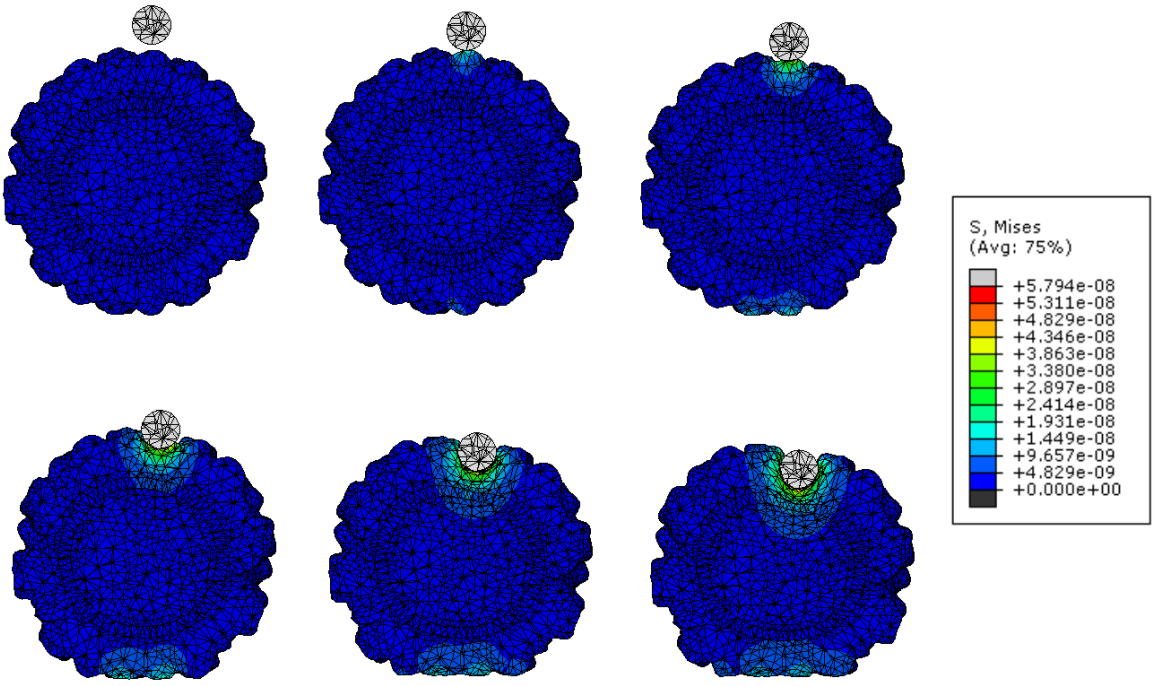

Figure 3-12: *Cross-sectional view of the computational simulation from the start of the simulation to the maximum indentation of the VLP illustrating the deformation and associated colour-coded stress distribution in the VLP. The model was calibrated for a Poisson's ratio of ν_v = 0.3, 0.35 and 0.4. The indenter is positioned 1.265 nm above the VLP, and the maximum indenter load was 22 nm. The VLP (blue) is indented by the indenter (grey). The colour-coded mechanical stress scale (MPa) is indicated on the right.*

The calibration of the model for a Poisson's ratio of the VLP of ν_v = 0.3 predicted an elastic modulus of the VLP of E_v = 4 MPa. With E_v and a spring constant of k_v = 0.035 N/m based on experiments, the model predicted an indentation depth of 6.24 nm and 14.73 nm at indentation force (F_i) of 0.1 nN and 0.4 nN, respectively. The FD curves for E_v = 4 MPa for ν_v = 0.3, 0.35 and 0.4 are illustrated in Figure 3-13 (a). The calibration of the model for ν_v = 0.35 predicted an elastic modulus of the VLP of E_v = 3.5 MPa. With E_v and a spring constant of k_v = 0.035 N/m based on experiments, the model predicted an indentation depth of 6.23 nm and 14.77 nm at F_i = 0.1 nN and 0.4 nN, respectively. The FD curves for E_v = 3.5 MPa for ν_v = 0.3, 0.35 and 0.4 are illustrated in Figure 3-13 (b). The calibration of the model for ν_v = 0.4 predicted an elastic modulus of the VLP of E_v = 2.9 MPa. With E_v and a spring

constant of k_v = 0.035 N/m based on experiments, the model predicted an indentation depth of 6.26 nm and 14.85 nm at F_i = 0.1 nN and 0.4 nN, respectively. The FD curves for E_v = 2.9 MPa for ν_v = 0.3, 0.35 and 0.4 are illustrated in Figure 3-13 (c).

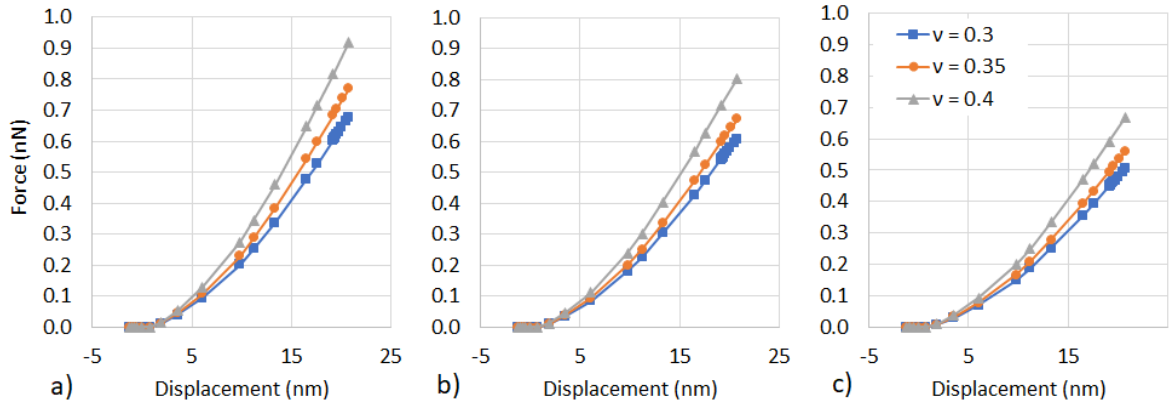

Figure 3-13: *Force-displacement curves for the predicted elastic moduli. The FD curves for a) E_v = 4 MPa, b) E_v = 3.5 MPa and c) E_v = 2.9 MPa for ν_v = 0.3, 0.35 and 0.4. The curves for ν_v = 0.3, 0.35 and 0.4 are indicated with blue squares, oranges circles and grey triangles, respectively.*

Figure 3-14 illustrates the FD curves of the *in vitro* and *in silico* results. The curves included from the *in silico* for E_v = 4 MPa and ν_v = 0.3, E_v = 3.5 MPa and ν_v = 0.35, and E_v = 2.9 MPa and ν_v = 0.4.

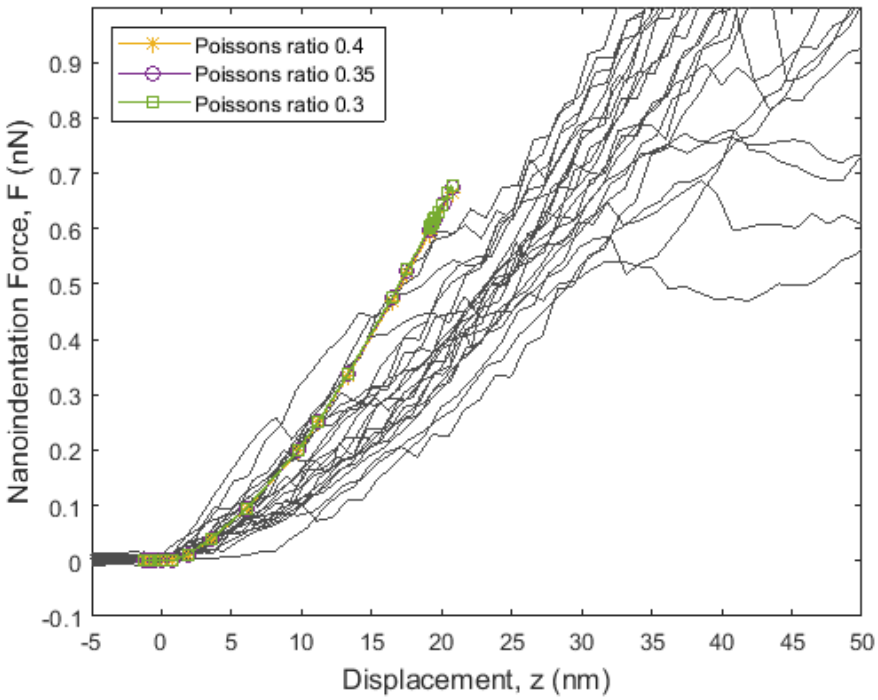

Figure 3-14: *Force-displacement curves for the nanoindentation experiments and computational simulations. The FD curves representing the experimental results for the VLPs tested in PBS are indicated by the thin lines. The FD curves from the computational simulations are indicated by the thick lines. The curves from the computational simulations represented for E_v = 2.9 MPa and ν_v = 0.4 (yellow stars), E_v = 3.5 MPa and ν_v = 0.35 (purple circles), and E_v = 4 MPa and ν_v = 0.3 (green squares).*

The elastic modulus of the chikungunya virus was also approximated using the thin shell model (Landau and Lifshitz 1986). The radius and thickness of the virus were determined from Figure 2-1 as 34.2 nm and 14.1 nm, respectively. The elastic modulus was determined to be E_t = 6.0 MPa.

3.4. Discussion

3.4.1. Development of 3D Geometric Models

The 3D geometric model of the VLP was successfully reconstructed using UCSF Chimera from cryo-EM images of a chikungunya VLP generated by Jin *et al.* (2015). The model was processed from a shell to a solid, continuous structure and then meshed in Simpleware ScanIP. The mesh comprised 63,439 tetrahedral elements.

3.4.2. Finite Element Modelling

The finite element model to simulate AFM indentation of the chikungunya virus was successfully constructed and calibrated for the spring constant of 0.035 N/m. The virus material was modelled as linear elastic and the Poisson's ratio (ν_v) chosen was 0.3 – 0.4 because the virus was slightly compressible. The elastic modulus obtained for ν_v = of 0.3, 0.35 and 0.4 was E_v = 4.0, 3.5 and 2.9 MPa, respectively. This indicates that the elastic modulus of the virus was indirectly proportional to the Poisson's ratio, therefore as ν_v increases, the VLP becomes softer. The results also indicated that for a constant ν_v, the VLP behaves softer as the E_v decreases. For a constant E_v, the VLP behaves softer as ν_v decreases.

The elastic modulus of the virus calculated using the thin shell model was E_t = 6.0 MPa. This value corresponds with the elastic moduli determined *in silico* (E_v = 2.9 – 4.0 MPa).

Limited information on chikungunya virus prevents comparison of the elastic modulus to literature; however, the elastic modulus was comparable to other viruses, as shown in Table 3-3. The elastic modulus of the enveloped viruses, HIV and influenza virus, and non-enveloped viruses, CCMV and Bacteriophage HK97, were determined. The elastic modulus of the viral capsid of the enveloped viruses, HBV, was also determined. The elastic modulus of the chikungunya virus *in silico* (E_v = 2.9 – 4.0 MPa) and using the thin shell model (E_t = 6.0 MPa) was at least two orders of magnitude lower than other viruses.

The studies evaluating the elastic moduli of other viruses (Table 3-3) either used the thin shell model or modelled the viruses as thin spherical shells. However, *in silico* chikungunya virus had a solid

spherical geometry and the thickness of the virus assumed for the thin shell model was significantly larger than the thickness of other enveloped viruses. It is hypothesized that the differences in virus model geometry and shell thickness may cause the disparities in the magnitude of the elastic modulus however each virus has individual material properties and large differences can be expected, as shown between influenza virus and CCMV.

Table 3-3: Elastic modulus of chikungunya virus compared to other viruses.

Virus name	Elastic modulus (MPa)	Reference
Chikungunya virus (CHIKV)	2.9 – 6.0	
Human immunodeficiency virus (HIV)	440	(Kol *et al.* 2007)
Cowpea chlorotic mottle virus (CCMV)	250	(Wilts *et al.* 2015)
Influenza virus	1,000	(Schaap *et al.* 2012)
Bacteriophage HK97	900	(Roos *et al.* 2012)
Hepatitis B virus (HBV)	260	(Roos *et al.* 2010)

The material behaviour of the VLP was modelled as linear elastic; however, the relationship between the indentation force and displacement was not linear. This could be caused by the interaction between the cantilever surface and the irregular 3D topographical VLP surface as a result of the presence of the glycoproteins (Roos *et al.* 2010). The nonlinear indentation behaviour predicted by the computational simulations corresponds with the indentation behaviour observed in the experimental results.

The indentation of the VLPs associated with indentation forces of 0.1 and 0.4 nN was higher for the nanoindentation experiments (7.54 nm and 20.07 nm, respectively) compared to the FE simulations (6.23 – 6.26 nm and 14.73 – 14.85 nm, respectively). This indicated that the FE model, which consisted of a solid homogenous geometry for the VLP, behaved stiffer than the VLPs during experimental analysis, which has a heterogeneous geometry.

4. Conclusions and Recommendations

The project aimed to study experimentally and computationally the mechanical properties and morphology of chikungunya as an enveloped virus to enable investigations of mechanobiological interactions between virions and host cells involved in the infection process.

The objectives derived for the project were:

1. To study the mechanical properties of chikungunya virions and how these are affected by the environment.

   The hypothesis related to this objective was that a decrease in pH in the endosomal environment would result in increased stiffness of the chikungunya virions.
2. To develop 3D computational geometries and finite element models of chikungunya virions that can be used for computational investigations of the mechanics of chikungunya virions, and more generally enveloped virions, and their interactions with host cells.

The objectives were met using various assessments, and this section covers the conclusions from these assessments and recommendations for future studies.

4.1. Conclusions

4.1.1. Mechanical Assessment of Chikungunya Virions

The mechanical assessment of the chikungunya virus was undertaken using AFM. AFM allows for the imaging and indenting of individual virions *in vitro,* which was used to ascertain the height and spring constant of the virions. The chikungunya virus strain used was the S27-African prototype.

The mechanical assessment indicated significant differences in the height ($p < .001$) and spring constant ($p = .024$) between the virions tested in PBS and MES. PBS represented the neutral extracellular environment with pH 7.4. MES represented the acidic endosomal environment with pH 6.0. virions in the acidic environment that promotes fusion (MES) were found to be smaller (h_v = 46.0 ± 0.8 nm) and stiffer (k_v = 0.047 ± 0.003 N/m) compared to the virions in an environment with neutral pH (h_v = 57.8 ± 0.6 nm and k_v = 0.035 ± 0.003 N/m).

It is proposed that the acidification of the buffer, representing an environment conducive to fusion, caused the full or partial dissociation of the glycoproteins. However, due to the way the glycoproteins are embedded in the membrane and the hydrophobic properties of the membrane, the membrane

disassociates along with the glycoproteins. It is proposed that this resulted in the significant reduction in the height of the virions tested in MES compared to those tested in PBS. Studies such as Kol *et al.* (2007) have shown that the presence or absence of glycoproteins has a significant impact on the spring constant. It is hypothesized that the dissociation, whether full or partial, of the glycoproteins of the virions in the acidic environment (MES), caused a significant increase in the spring constant. The mechanical assessment also sheds light into the possible mechanical and conformational changes the virus may undergo during the infection process.

4.1.2. Development of 3D Geometric Model and Computational Simulations of Chikungunya Virions

Image-based 3D geometric and finite element models were developed, and computational simulations of AFM nanoindentation experiments of chikungunya virus were successfully completed. The 3D geometric model of a chikungunya VLP was reconstructed using cryo-EM data generated by Jin *et al.* (2015). The finite element model was used in an analysis evaluating the indentation behaviour of chikungunya virus. The *in silico* analysis simulated the AFM nanoindentation test and calibrated the elastic modulus (E_v) and Poisson's ratio (ν_v) of the computational model to the spring constant of the virus obtained *in vitro* in the experiments in PBS. The Poisson's ratio was chosen as ν_v = 0.3, 0.35 and 0.4. The elastic modulus was determined as E_v = 4, 3.5 and 2.9 MPa, respectively. The E_v decreased as the ν_v increased. This shows that the virus becomes softer as the ν_v increased. The assessment also indicated that when the ν_v remained constant, the E_v decreases and the VLP becomes softer. When the E_v remained constant, the spring constant decreases making the virus softer as ν_v decreases. The elastic modulus of the virus determined using the thin shell model was E_t = 6.0 MPa, which corresponds with the elastic moduli found from FEM. The average indentation depth at an indentation force of 0.1 and 0.4 nN was greater *in vitro* than *in silico*. This indicated that the FE analysis modelled the virus as stiffer than what was found experimentally. This could be caused by the differences in the geometry of the virus *in vitro* and *in silico*: non-solid, heterogenous geometry *in vitro* and solid, homogenous geometry *in silico*. The FE model will also enable further studies into the mechanics of VLPs during the infection process.

4.2. Recommendations

4.2.1. Imaging of Chikungunya Virions

An investigation is needed to study the morphology of the virions tested in PBS and MES during the AFM experiments. Fluorescence microscopy can be used to visualise the membrane and glycoproteins. The glycoproteins can be stained, and the presence or absence of the spikes can be detected. Virions

can also be imaged using electron microscopy (EM) which may allow visualisation of the structures at a higher resolution. Such an investigation can bring an understanding of the conformational changes chikungunya virus undergoes in preparation for entering a host cell. This investigation may also shed light into the role glycoproteins play with the stiffness shift of the virus.

4.2.2. Investigation of Virion Cross-Section

The experiments showed a reduction in VLP height due to the indentation test. It was suggested that the VLPs plastically deform under the load of the cantilever. An investigation of the cross-sectional VLP width could be conducted to determine if the VLPs may have expanded or flattened after the indentation test.

4.2.3. Expand Experimental Sample Size

The mechanical assessment indicated that there was no correlation between the VLP height and spring constant; however, only 23 and 37 VLPs were analysed in PBS and MES, respectively. Expanding the experimental sample size can give a better indication of a relationship that may exist between the height and spring constant.

4.2.4. Standardisation of Testing Environment

The type of buffer solution was altered due to the pH requirements of the testing environment and the active pH range for the respective buffers. It was proposed that the change in height and spring constant was attributed to the change in pH. However, the change in the type of buffer may have influenced the results. Further mechanical assessments could involve the use of a buffer with an active pH range that covers both testing environments. This can limit the factors that can influence the results.

4.2.5. Variation of Constitutive Law

The computational simulation was governed by the isotropic linear elastic material constitutive laws. The nonlinear elastic behaviour of the VLP model could be attributed to the 3D topographical detail of the reconstructed VLP. Other studies such as Ahadi *et al.* (2009) and Roos *et al.* (2010) modelled virus behaviour as hyperelastic with neo-Hookean laws. This allowed the studies to capture the nonlinear behaviour of the virion independent of topographical detail. Adoption of similar constitutive laws in further investigations may provide models which have a strong correlation with experimental data.

4.2.6. Variation of Material Properties

In the current model, the same material properties were assigned to the entire reconstructed VLP. The wild-type (WT) virions are composed of various structure which may have varying material properties. A further investigation involving assigning distinct material properties to different structures may provide insight into the material properties of the structures of the virions and the role each plays in regulating the stiffness throughout the lifecycle.

4.2.7. Refinement of the Internal Virion Geometry

In the current model, the VLP had a simplified internal geometry; however, the WT virion consists of various structures. Refining the internal geometry of the reconstructed model to represent the geometry of the WT virions may bring a better understanding of the interaction between the virion structures

5. References

Ahadi A, Colomo J, Evilevitch A. *Three-dimensional simulation of nanoindentation response of viral capsids. Shape and size effects*. J Phys Chem B 2009, **113**(11): 3370-8.

Albers RRW. Cell membrane structures and functions, 2012.

Arkhipov A, Roos WH, Wuite GJ, Schulten K. *Elucidating the mechanism behind irreversible deformation of viral capsids*. Biophys J 2009, **97**(7): 2061-9.

Baró AM, Reifenberger RG. Atomic force microscopy in liquid: Biological applications, 2012.

Bordi L, Caglioti C, Lalle E, Castilletti C, Capobianchi MR. *Chikungunya and its interaction with the host cell*. Curr Trop Med Rep 2015, **2**(1): 22-9.

Centers for Disease Control and Prevention. *Chikungunya virus*. Retrieved 2 October, 2017, from https://www.cdc.gov/chikungunya/index.html.

Centers for Disease Control and Prevention. *About zika*. Retrieved 12 November, 2019, from https://www.cdc.gov/.

Centers for Disease Control and Prevention. *Geographic distribution: Where has chikungunya virus been found?* , from https://www.cdc.gov/chikungunya/geo/index.html.

Chen Z, Sun L, Zhang Z, Fokine A, Padilla-Sanchez V, Hanein D, Jiang W, Rossmann MG, Rao VB. *Cryo-em structure of the bacteriophage t4 isometric head at 3.3-a resolution and its relevance to the assembly of icosahedral viruses*. Proc Natl Acad Sci U S A 2017, **114**(39): E8184-E93.

Chou T. *Stochastic entry of enveloped viruses: Fusion versus endocytosis*. Biophys J 2007, **93**(4): 1116-23.

Cross KJ, Burleigh LM, Steinhauer DA. *Mechanisms of cell entry by influenza virus*. Expert Rev Mol Med 2001, **3**(21): 1-18.

Engineering Toolbox. *Young's modulus - tensile and yield strength for common materials*. from https://www.engineeringtoolbox.com/young-modulus-d_417.html.

Engineering Toolbox. *Poisson's ratio*. from https://www.engineeringtoolbox.com/poissons-ratio-d_1224.html.

Gibbons MM, Klug WS. *Nonlinear finite-element analysis of nanoindentation of viral capsids*. Phys Rev E Stat Nonlin Soft Matter Phys 2007, **75**(3 Pt 1): 031901.

Goni FM. *The basic structure and dynamics of cell membranes: An update of the singer-nicolson model*. Biochim Biophys Acta 2014, **1838**(6): 1467-76.

Greber UF. *How cells tune viral mechanics--insights from biophysical measurements of influenza virus*. Biophys J 2014, **106**(11): 2317-21.

Hoornweg TE, Van Duijl-Richter MK, Ayala Nunez NV, Albulescu IC, Van Hemert MJ, Smit JM. *Dynamics of chikungunya virus cell entry unraveled by single-virus tracking in living cells*. J Virol 2016, **90**(9): 4745-56.

Jin J, Liss NM, Chen DH, Liao M, Fox JM, Shimak RM, Fong RH, Chafets D, Bakkour S, Keating S, Fomin ME, Muench MO, Sherman MB, Doranz BJ, Diamond MS, Simmons G. *Neutralizing monoclonal antibodies block chikungunya virus entry and release by targeting an epitope critical to viral pathogenesis*. Cell Rep 2015, **13**(11): 2553-64.

Katz G, Benkarroum Y, Wei H, Rice WJ, Bucher D, Alimova A, Katz A, Klukowska J, Herman GT, Gottlieb P. *Morphology of influenza b/lee/40 determined by cryo-electron microscopy*. PLoS One 2014, **9**(2): e88288.

Kielian M, Chanel-Vos C, Liao M. *Alphavirus entry and membrane fusion*. Viruses 2010, **2**(4): 796-825.

Kol N, Gladnikoff M, Barlam D, Shneck RZ, Rein A, Rousso I. *Mechanical properties of murine leukemia virus particles: Effect of maturation*. Biophys J 2006, **91**(2): 767-74.

Kol N, Shi Y, Tsvitov M, Barlam D, Shneck RZ, Kay MS, Rousso I. *A stiffness switch in human immunodeficiency virus*. Biophys J 2007, **92**(5): 1777-83.

Kruse E. *Studying the mechanics of enveloped viruses and their interactions with the host cell*, University of Cape Town, 2017: 1-89.

Kuo SC, Chen YJ, Wang YM, Tsui PY, Kuo MD, Wu TY, Lo SJ. *Cell-based analysis of chikungunya virus e1 protein in membrane fusion*. J Biomed Sci 2012, **19**: 44.

Landau LD, Lifshitz EM. Theory of elasticity. Oxford, Elsevier, 1986.

Li S, Sieben C, Ludwig K, Hofer CT, Chiantia S, Herrmann A, Eghiaian F, Schaap IA. *Ph-controlled two-step uncoating of influenza virus*. Biophys J 2014, **106**(7): 1447-56.

Lua LH, Connors NK, Sainsbury F, Chuan YP, Wibowo N, Middelberg AP. *Bioengineering virus-like particles as vaccines*. Biotechnol Bioeng 2014, **111**(3): 425-40.

Marchetti M, Wuite G, Roos WH. *Atomic force microscopy observation and characterization of single virions and virus-like particles by nano-indentation*. Curr Opin Virol 2016, **18**: 82-8.

Michel JP, Ivanovska IL, Gibbons MM, Klug WS, Knobler CM, Wuite GJ, Schmidt CF. *Nanoindentation studies of full and empty viral capsids and the effects of capsid protein mutations on elasticity and strength*. Proc Natl Acad Sci U S A 2006, **103**(16): 6184-9.

Murakami T, Ablan S, Freed EO, Tanaka Y. *Regulation of human immunodeficiency virus type 1 env-mediated membrane fusion by viral protease activity*. J Virol 2004, **78**(2): 1026-31.

Nanosensors™. *Uniqprobe™ uniform quality spm probe – contact or dynamic mode for biology in dynamic (ac) mode*. 2020, from https://www.nanosensors.com/uniqprobe-uniform-quality-contact-or-dynamic-mode-for-biology-in-dynamic-ac-mode-afm-tip-qp-BioAC.

Nicolson G. *Fluid-mosaic membrane structure: From cellular control and domains to extracellular vesicles*, 2016: 1-23.

Noda T. *Native morphology of influenza virions*. Front Microbiol 2011, **2**: 269.

Noranate N, Takeda N, Chetanachan P, Sittisaman P, A AN, Anantapreecha S. *Characterization of chikungunya virus-like particles*. PLoS One 2014, **9**(9): e108169.

Pang H-B, Hevroni L, Kol N, Eckert D, Tsvitov M, Kay M, Rousso I. *Virion stiffness regulates immature hiv-1 entry*. Retrovirology 2013, **10**(1): 4.

Pettersen E, Goddard T, Huang C, Couch G, Greenblatt D, Meng E, Ferrin T. *Ucsf chimera--a visualization system for exploratory research and analysis.* . J Comput Chem 2004, **25**(13): 1605-12.

Pietzsch J. *Mind the membrane*, Nature Publishing Group, 2004.

Protein Data Bank Japan. *Cryo-em of chikv vlp*. 2020, from https://www.ebi.ac.uk/pdbe/entry/emdb/EMD-6466/.

Roos WH. *How to perform a nanoindentation experiment on a virus*. Methods Mol Biol 2011, **783**: 251-64.

Roos WH, Gertsman I, May ER, Brooks CL, 3rd, Johnson JE, Wuite GJ. *Mechanics of bacteriophage maturation*. Proc Natl Acad Sci U S A 2012, **109**(7): 2342-7.

Roos WH, Gibbons MM, Arkhipov A, Uetrecht C, Watts NR, Wingfield PT, Steven AC, Heck AJ, Schulten K, Klug WS, Wuite GJ. *Squeezing protein shells: How continuum elastic models, molecular dynamics simulations, and experiments coalesce at the nanoscale*. Biophys J 2010, **99**(4): 1175-81.

San Jose Delta. *Quartz material properties data*. from https://www.sanjosedelta.com/quartz.html.

Schaap IA, Eghiaian F, Des Georges A, Veigel C. *Effect of envelope proteins on the mechanical properties of influenza virus*. J Biol Chem 2012, **287**(49): 41078-88.

Schwartz O, Albert ML. *Biology and pathogenesis of chikungunya virus*. Nat Rev Microbiol 2010, **8**(7): 491-500.

Sigma-Aldrich. *Buffer reference center*. Retrieved 25 June, 2020, from https://www.sigmaaldrich.com/life-science/core-bioreagents/biological-buffers/learning-center/buffer-reference-center.html.

Sirohi D, Chen Z, Sun L, Klose T, Pierson TC, Rossmann MG, Kuhn RJ. *The 3.8 a resolution cryo-em structure of zika virus*. Science 2016, **352**(6284): 467-70.

Snijder J, Ivanovska IL, Baclayon M, Roos WH, Wuite GJL. *Probing the impact of loading rate on the mechanical properties of viral nanoparticles*. Micron 2012, **43**: 1343-50.

Sourisseau M, Schilte C, Casartelli N, Trouillet C, Guivel-Benhassine F, Rudnicka D, Sol-Foulon N, Le Roux K, Prevost MC, Fsihi H, Frenkiel MP, Blanchet F, Afonso PV, Ceccaldi PE, Ozden S, Gessain A, Schuffenecker I, Verhasselt B, Zamborlini A, Saib A, Rey FA, Arenzana-Seisdedos F, Despres P, Michault A, Albert ML, Schwartz O. *Characterization of reemerging chikungunya virus*. PLoS Pathog 2007, **3**(6): e89.

Sun S, Xiang Y, Akahata W, Holdaway H, Pal P, Zhang X, Diamond MS, Nabel GJ, Rossmann MG. *Structural analyses at pseudo atomic resolution of chikungunya virus and antibodies show mechanisms of neutralization*. Elife 2013, **2**: e00435.

Tang BL. *The cell biology of chikungunya virus infection*. Cell Microbiol 2012, **14**(9): 1354-63.

Van Duijl-Richter MK, Blijleven JS, Van Oijen AM, Smit JM. *Chikungunya virus fusion properties elucidated by single-particle and bulk approaches*. J Gen Virol 2015a, **96**(8): 2122-32.

Van Duijl-Richter MK, Hoornweg TE, Rodenhuis-Zybert IA, Smit JM. *Early events in chikungunya virus infection-from virus cell binding to membrane fusion*. Viruses 2015b, **7**(7): 3647-74.

Veesler D, Johnson JE. *Virus maturation*. Annu Rev Biophys 2012, **41**: 473-96.

Vu DM, Jungkind D, Angelle Desiree L. *Chikungunya virus*. Clin Lab Med 2017, **37**(2): 371-82.

Wikan N, Sakoonwatanyoo P, Ubol S, Yoksan S, Smith DR. *Chikungunya virus infection of cell lines: Analysis of the east, central and south african lineage*. PLoS One 2012, **7**(1): e31102.

Wilts BD, Schaap IaT, Schmidt CF. *Swelling and softening of the cowpea chlorotic mottle virus in response to ph shifts*. Biophys J 2015, **108**(10): 2541-9.

World Health Organization. *Chikungunya*. Retrieved 3 October, 2017, from http://www.who.int/mediacentre/factsheets/fs327/en/.

World Health Organization. *Chikungunya – congo*. Retrieved 1 April, 2020, from https://www.who.int/csr/don/01-may-2019-chikungunya-congo/en/.

World Health Organization. *Dengue and severe dengue*. Retrieved 12 November, 2019, from https://www.who.int/news-room/fact-sheets/detail/dengue-and-severe-dengue.

Wyma DJ, Jiang J, Shi J, Zhou J, Lineberger JE, Miller MD, Aiken C. *Coupling of human immunodeficiency virus type 1 fusion to virion maturation: A novel role of the gp41 cytoplasmic tail*. J Virol 2004, **78**(7): 3429-35.

Yap ML, Klose T, Urakami A, Hasan SS, Akahata W, Rossmann MG. *Structural studies of chikungunya virus maturation*. Proc Natl Acad Sci U S A 2017, **114**(52): 13703-7.

Zeltins A. *Construction and characterization of virus-like particles: A review*. Mol Biotechnol 2013, **53**(1): 92-107.

Zhang Y, Dudko OK. *Statistical mechanics of viral entry*. Physical Review Letters 2015, **114**.